

THESIS FOR THE DEGREE OF DOCTOR OF PHILOSOPHY

Large-Eddy Simulation of Gasoline Fuel Spray Injection at Ultra-High Injection Pressures

Sandip Wadekar



Department of Mechanics and Maritime Sciences
CHALMERS UNIVERSITY OF TECHNOLOGY
Göteborg, Sweden 2021

Large-Eddy Simulation of Gasoline Fuel Spray Injection at Ultra-High Injection Pressures

SANDIP WADEKAR

ISBN 978-91-7905-492-2

© SANDIP WADEKAR , 2021.

Doktorsavhandlingar vid Chalmers tekniska högskola

Ny serie nr 4959

ISSN0346-718X

Department of Mechanics and Maritime Sciences

Chalmers University of Technology

SE-412 96 Göteborg, Sweden

Telephone + 46 (0) 31 – 772 1000

Cover: by Sandip Wadekar

Typeset by the author using L^AT_EX.

Printed by Chalmers Reproservice

Göteborg, Sweden 2021

To my parents, who brought me here

Abstract

Gasoline direct injection is a state-of-the-art technique that reduces hydrocarbon and particulate emissions. However, further improvement is needed to meet current as well as future emission regulations. A prominent solution is to increase the fuel injection pressure which allows faster fuel droplet atomization, quick evaporation and improves fuel-air mixture formation under realistic engine conditions. In this work, the gasoline fuel injection process at ultra-high injection pressures ranging from 200 to 1500 bar was analyzed using numerical models. In particular, the Large-Eddy Simulation (LES) method, with the standard Smagorinsky turbulence model, was utilized using the Eulerian formulation for the continuous phase. The discrete droplet phase was treated using a Lagrangian formulation together with spray sub-models. In the first part of study, spray was injected into an initially quiescent constant volume chamber using two different nozzle hole shape geometries: divergent and convergent. The numerical results were calibrated by reproducing experimentally observed liquid penetration length and efforts were made to understand the influence of ultra-high injection pressures on spray development. The calibrated models were then used to investigate the impact of ultra-high injection pressures on mean droplet sizes, droplet size distribution, spray-induced large-scale eddies and entrainment rate. The results showed that, at ultra-high injection pressures, the mean droplet sizes were significantly reduced and the droplets achieving very high velocities. Integral length scales of spray-induced turbulence and air entrainment rate were better for the divergent-shaped injector, and considerably larger at higher injection pressures compared to lower ones.

In the second part of the study, four consecutive full-cycle cold flow LES simulations were carried out to generate realistic turbulence inside the engine cylinder. The first three cycles were ignored, with the fourth cycle being used to model the injection of the fuel using the divergent-shaped injector only (which was found to be better in the previous part of this study) at different injection pressures. In addition to the continuous gas phase (Eulerian) and the dispersed liquid (Lagrangian), the liquid film feature (Finite-Area) was used to model the impingement of fuel spray on the engine walls and subsequent liquid film formation. The simulation results

were used to evaluate spray-induced turbulence, fuel-air mixing efficiency and the amount of liquid mass deposited on the walls. The limitation of the high-pressure injection technique with respect to liquid film formation was optimized using a start of injection (SOI) sweep. Overall results showed that the mixing efficiency increased at high injection pressure and that SOI should occur between early injection and late injection to optimize the amount of mass being deposited on the engine walls.

Keywords: high pressure fuel injection, spray-wall interaction, spray-turbulence interaction, GDI engine, LES

Acknowledgments

It's been a great time learning, working and having fun in the division and in the time period altogether that I have spent working so far. For this I have to acknowledge a lot of people. First I would like to thank my main supervisor Michael Oevermann and CERC director Ingemar Denbratt for giving me the opportunity to work in this project. I thank again Michael Oevermann for the fruitful discussions and all the support not only in the project but also for other related stuff. I also thank my co-supervisor Andrei Lipatnikov for his guidance in various ways. Its only me who knows how much I irritate you by asking same questions again and again but you was always be calm and respond nicely all the time.

I would like acknowledge the project members, Lucien Koopmans, Petter Dahlander, Johan Dillner, Ayolt Helmantel and Akichika Yamaguchi. You often gave me critical feedbacks and advices in the project meetings.

Apart from this I want to acknowledge all my fellow PhD students in the division who were there during good and tough times for chats during fikas, lunches and afterworks and played an important role during the period I worked so far. I would like to special thank to Andreas Nygren aka my trouble shooter, for his help on various problem related to Linux. I want to acknowledge the good times and conversations I had with research engineers and teaching/research staff who contributed to make a good working environment for me. Indeed, I thank Elenor for organizing lovely Christmas dinners, summer lunches and other support works.

Last but not the least I cannot conclude without acknowledging my parents, my brother and my wife for their endless support.

Sandip Wadekar
Göteborg, May 2021

List of Publications

This thesis is based on the following appended papers:

Paper 1. Sandip Wadekar and Michael Oevermann "Large-Eddy Simulation of Spray-Turbulence-Wall interaction in a Gasoline Direct Injection Engine at Ultra-high Injection Pressures" submitted to *International Journal of Multiphase Flow* (2021).

Paper 2. Sandip Wadekar, Akichika Yamaguchi, and Michael Oevermann "Large-Eddy Simulation Study of Ultra-High Fuel Injection Pressure on Gasoline Sprays" in *Flow Turbulence and Combustion* (2020) , doi: <https://doi.org/10.1007/s10494-020-00231-0>.

Paper 3. Sandip Wadekar, Akichika Yamaguchi, and Michael Oevermann "Large-eddy simulation on the effects of fuel injection pressure on the gasoline spray characteristics" in *SAE International Powertrains Fuels and Lubricants* (2019), San Antonio, USA, doi: <https://doi.org/10.4271/2019-01-0060>.

Other related publications:

Paper 4. Sandip Wadekar, Peter Janas, and Michael Oevermann, "Large-eddy simulation study of combustion cyclic variation in a lean-burn spark ignition engine" in *Applied Energy* (2019) , doi: <https://doi.org/10.1016/j.apenergy.2019.113812>.

Paper 5. Sandip Wadekar, Peter Janas, and Michael Oevermann "A multi-cycle Large-Eddy Simulation study of combustion cyclic variation in a SI-engine" in *11th Mediterranean Combustion Symposium* (2019), Tenerife, Spain.

Paper 6. Sandip Wadekar, Michael Oevermann, and Andrei Lipatnikov, "Large Eddy Simulation of Stratified Combustion in Spray-Guided Direct Injection Spray-ignition engine" in *WCXTM: SAE World Congress Experience* (2018), Detroit, MI, USA, doi: <https://doi.org/10.4271/2018-01-1420>.

Contents

Abstract	v
Acknowledgments	vii
List of Publications	ix
I Introductory chapters	1
1 Introduction	3
1.1 Motivation	4
1.2 Challenges	5
1.3 Objectives and Thesis Outline	8
2 Spray Fundamentals	11
2.1 Spray in Engine	11
2.2 Multiphase Flow Modeling	12
2.2.1 Interaction Between the Phases	13
3 Numerical Modeling	15
3.1 Governing Equations	15
3.1.1 Continuity Equation	17
3.1.2 Momentum Equation	17
3.1.3 Energy Equation	19
3.1.4 Constitutive Equation	20
3.2 Turbulence Modeling	21
3.2.1 Large Eddy Simulation	25
3.3 Spray Modeling	27
3.3.1 Liquid Injection Model	27
3.3.2 Droplet Motion	28
3.3.3 Secondary Droplet Breakup Model	29

3.3.4	Stochastic Droplet Dispersion Model	32
3.3.5	Droplet Evaporation Model	33
3.3.6	Droplet Tracking Model	34
3.4	Spray-Wall Interaction	35
3.4.1	Liquid-film Modeling	37
3.5	Numerical Solution Algorithm	39
4	Results and Discussion	41
4.1	Constant Volume Spray Chamber	41
4.1.1	Nozzle Design	41
4.1.2	Boundary Condition and Numerical Setup	42
4.1.3	Result Highlights	43
4.2	Optical GDI Engine	50
4.2.1	Mesh Handling and Mesh Motion	50
4.2.2	Boundary Condition and Numerical Setup	52
4.2.3	Result Highlights	53
5	Conclusion and Outlook	63
6	Future Work	65
7	Summary of Publications	67
	Appendix	77
	Bibliography	80
II	Appended papers	89

Part I

Introductory chapters

Chapter 1

Introduction

Combustion has been a key technology for transportation since the last century. Currently, there are more than 1.2 billion combustion engine vehicles driving all over the world. Despite their central role in shaping the modern world, both socially and economically, serious concerns have been raised with regard to the environmental impact of the gaseous and particulate emissions from such engines. Of particular concern are CO₂ emissions, that have greatly contributed to global warming. Combustion generated pollutants reduce the air quality in urban areas. Consequently, legislatures around the world are introducing increasingly strict regulations aimed at reducing the volume of hazardous emissions into the environment. For instance, the European Union has implemented legislation limiting the fleet average CO₂ emissions of vehicles to 130 g/km (depending on vehicle weight) in 2015 [1], see Fig. 1.1. This limit reduced to 95 g/km in 2020-21 and then a further reduction is expected to 68-78 g/km in 2025. Now, in addition to CO₂, a limit on particulate emissions has also been imposed. Similar regulations have been, or will be, implemented in other countries. To meet these requirements, vehicle manufacturers are investigating a range of strategies to reduce emissions, including geometrical improvement (downsizing), advanced injection methods (direct injection, charge stratification), lean combustion, turbocharging, variable valve timing etc. However, these techniques increase the complexity of engines and typically offer only marginal benefits.

To comply with these regulations, vehicle manufacturers are exploring alternative approaches, such as replacing emission generating internal combustion engines with battery-powered electric power trains, which emit no harmful pollutants directly. This could be a viable solution if the electricity used to power the vehicles is generated from renewable sources. However, the operational capacity and working lifespan of currently available batteries are very limited, and the environmental friendly disposal

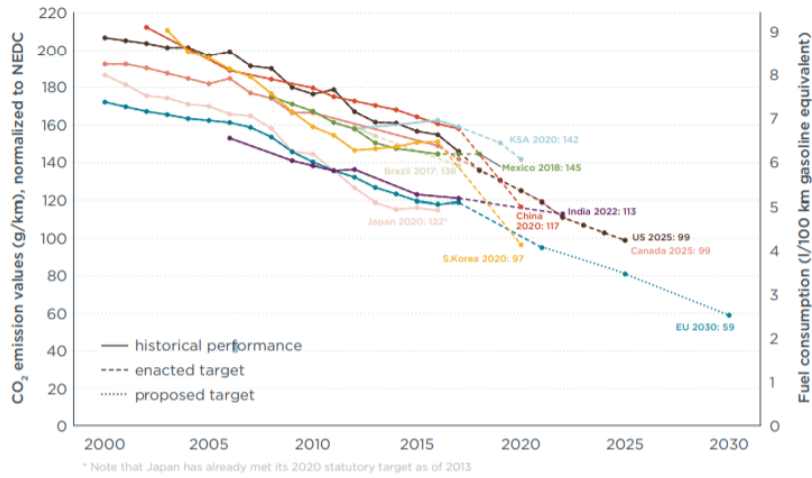


Figure 1.1: Global CO_2 regulations for new passenger cars [2].

of used batteries is also an issue. Therefore, the complete replacement of internal combustion engines with electric power trains is not currently a promising global solution to environmental problems. An alternative possible solution could be a hybrid system that combines an electric motor and internal combustion engine. The hybrid vehicle can be considered as a transition technology until full electric vehicle technology has matured enough, including a charging station infrastructure and renewable energy sources. The complete replacement of internal combustion vehicles with electrically powered ones globally is unlikely to happen soon and therefore the combustion engine, also a part of hybrid vehicles, still has a major role to play and requires further improvement.

1.1 Motivation

Strict regulations concerning CO_2 and particulate emissions have promoted the introduction of cleaner and more efficient engines. To help comply with these regulations, a state-of-the-art technique called Gasoline Direct Injection (GDI) has been developed that significantly reduces hydrocarbon emissions [3] and fuel consumption. However, it also has a tendency to produce higher particulate emissions [4, 5] due to imperfect fuel-air mixture formation, an issue considered to be a main challenge with GDI engines.

One of the possible solutions to improve the fuel-air mixture is to increase the fuel injection pressure. A higher fuel injection pressure significantly improves the fuel-air mixture formation due to faster fuel atomization, reduces fuel droplet size

promoting faster evaporation and thus reduces soot emissions. It also promotes in-cylinder turbulence and air entrainment [6]. It has already been demonstrated elsewhere [7, 8]. Such benefits have led to fuel injection pressures in GDI systems continuously increasing since their introduction into the market in the late 1990s. At the beginning, first-generation fuel injection systems used injection pressures of 50-100 bar and supported stratified combustion. The sprays generated by these injectors were very sensitive to the engine's operating and thermodynamic conditions [9]. The motivation for increasing fuel injection pressure was the need to improve atomization and mixture formation, which was achieved using second generation spray-stratified combustion systems in 2006 [10]. Over the last decade, maximum fuel injection pressures have increased from 200 to 250 bar and, more recently, injection pressures up to 350 bar have been used, achieved through a common-rail system and smaller nozzles. Based on potential of high injection pressure, it is expected that fuel injection pressures will increase to 400 bar by 2022 and 600 bar by 2026. These increases, together with related injector modifications, such as changes in nozzle geometry and design, could increase engine efficiency by as much as 4 % [11].

1.2 Challenges

Two major factors controlling fuel-air mixing in GDI engines are the fuel injection pressure and the nozzle design. Some studies have been carried out into the effects of increasing injection pressure up to 500 bar [11, 12, 13, 14, 15, 16, 17, 18], however, few studies have investigated beyond 500 bar injection pressures [19, 20, 21]. Nauwerck et al. [22] measured the macroscopic spray characteristics, droplet sizes, the velocity of the spray droplets and surrounding air under injection pressures up to 500 bar. They concluded that the smallest droplet diameters and highest velocity gradient exist within the spray jet at the highest injection pressure. Matousek et al. [23] investigated the effect of injection pressure on particulate number (PN) and concluded that the PN was reduced by 50% at 300 bar compared to 200 bar injection pressure. Medina et al. [24] studied gasoline fuel sprays at injection pressures between 300 to 1500 bar as a function of chamber pressure using a high-speed imaging technique and concluded the spray characteristics. Buri et al. [25] demonstrated the effect of high-pressure fuel injection on mixture preparation and subsequent soot formation. The results showed that the injection duration and vaporization time were significantly reduced at 1000 bar compared to 200 bar injection pressure. At 200 bar injection pressure, the fuel mass is not completely mixed with air at the start of combustion, causing high soot emissions. A large number of previous studies on high

injection pressure have focused on macroscopic spray characteristics and emission data. However, fundamental and detailed descriptions of atomization characteristics, turbulence, air entrainment, wall-wetting and spatial distribution of equivalence ratio under ultra-high injection pressure are still needed. Some investigations [26, 27] have also been carried out on the effects of nozzle shape, however, its effect with high injection pressure is still unclear.

A major challenge of the high-pressure injection technique is to control the spray behavior and evolution. If spray shape and direction are not properly controlled, the spray hits the wall which is considered to be a major source of particulate and hydrocarbon emissions [28]. The spray developed at a high injection pressure has very high velocity which increases the risk of spray hitting the wall if not adequately controlled. Many strategies have been developed to reduce the fuel film. For instance, He et al. [29] suggested retarding the injection timing to avoid spray-wall interaction i.e. changing the start of injection (SOI) from 301° to 209° before top dead center. However, only low injection pressure conditions were investigated. Pan et al. [30] suggested increasing the wall temperature to facilitate faster evaporation of the liquid fuel film, however, this may lead to other issues. Therefore, a detailed understanding is needed to quantify the effect of injection pressure on liquid fuel film formation.

Another challenge in studying the higher-pressure injection technique is injector design. Due to the low lubricity and viscosity of gasoline, higher injection pressure causes problems of friction and wear [23], meaning that the maximum injection pressure used in GDI engines has remained at 250 bar for more than 10 years [31]. Moreover, in most of the previous studies, a conventional diesel injector is used (without any modification) with a relatively large L/D (nozzle thickness to hole diameter) ratio to withstand high pressures. A typical value of L/D ratio of a diesel injector is 8-9 but for a gasoline injector is 2-3. The large L/D ratio is undesirable because of its poor atomization characteristics.

In this study, gasoline sprays up to 1500 bar injection pressure were investigated with two different nozzle shapes: divergent and convergent. At such a high injection pressure, a conventional gasoline injector has issues of structural integrity and durability. Therefore, a prototype injector was designed based on a diesel injector, thank to DENSO CORPORATION JAPAN, with an L/D ratio of 5.45.

Typically, spray dynamics is a complex multi-scale physical phenomenon that is highly sensitive to injector nozzle geometry (cavitation), nozzle exit conditions (tur-

bulence), and fuel injection pressure. These conditions can change the atomization behavior and the physical processes of the spray after the nozzle exit. In the spray, near-nozzle flow typically consists of a liquid core (dense spray) and a dilute spray region. At the boundaries of the liquid core region, the spray breaks up into droplets. This process, known as primary breakup, is poorly understood because it involves a number of complex phenomena. In the dilute spray region, the liquid core further breaks up into smaller droplets, in a process called secondary breakup, which governs the transition from the dense to the dilute spray regimes. Secondary breakup is crucial for fuel-air mixture formation because efficient atomization increases the spray's surface area, enabling faster vaporization. All these processes become extremely complex at high injection pressures because the relevant events occur over such short timescales. A better understanding requires measurement techniques and numerical methods which can accurately resolve a detailed physics of these processes in space and time. Experiments of the near-nozzle region are extremely complicated because of the poor optical accessibility. It is also very challenging to isolate all the physical process. As a solution, computational fluid dynamics (CFD) simulation techniques offers an alternative way of studying these processes. The use of CFD is becoming more and more popular for studying fuel-air mixture formation inside engines.

At present, Direct Numerical Simulation (DNS) is the only computational method capable of resolving all length scales involved in the flow and atomization process. Unfortunately, its high computational cost largely restricts its use to academic test cases. An alternative method with lower computational costs, the Large-Eddy Simulation (LES) technique, has been widely used to simulate unsteady multiphase phenomena. LES can accurately capture intrinsic time- and space-dependent phenomena because it directly resolves large-scale turbulent structures and uses a model to describe sub-grid scale structures. In both commercial and non-commercial CFD codes, LES simulations are commonly performed using a Lagrangian particle tracking (LPT) approach to model the dispersed spray droplets. In this approach, groups of droplets with identical properties are represented as parcels (numerical particles) that are tracked using the Lagrangian method. This method represents the multi-dimensionality of fuel spray exceptionally well. Its accuracy strongly depends on the number of parcels per second in the simulated injection; large numbers of parcels are required to describe spray dynamics well. Due to the different scales involved in modeling the nozzle flow, atomization process and in-cylinder flow, it is challenging to consolidate all the phenomena (nozzle flow, in-cylinder turbulence, primary and secondary atomization) into a single CFD framework.

1.3 Objectives and Thesis Outline

The main objective of this thesis is to contribute to the understanding of the use of ultra-high injection pressures in gasoline direct injection engines. The LES simulations were used to model the fuel sprays, and consisted of discrete sets of Lagrangian parcels at pressures ranging from 200 to 1500 bar. At first, a constant volume chamber was used to analyze the impact of injection pressure on the spray characteristics. The aim of the numerical simulation was to quantify the mean droplet sizes, droplet size distribution, spray-induced turbulence and large-scale motion, and air entrainment at these higher pressures. Subsequently, a Chalmers optical research engine was used to mimic the fuel injection and fuel-air mixture formation process using full-cycle (except combustion) LES simulations. The focus of this part was on the effect of injection pressure on fuel-air mixture homogenization and liquid fuel film formation on the engine walls. The purpose of this part was to evaluate the gain in fuel-air mixture efficiency and to determine the quantity of fuel mass deposited on the engine walls. The overall aim was to facilitate the integration of these advanced injection systems into future gasoline direct injection engines.

In the scope of this thesis, two different experimental setups - a constant volume spray chamber and a Chalmers optical research engine - were used for LES simulations to address the following research questions/gaps:

- It is well known that higher injection pressures reduce the droplet sizes significantly. However, the exact sizes up to 1500 bar pressure are unknown. Also, it is unclear whether any limitations or cut-off points exist after which increasing the pressure has no effect.
- The spray at high injection pressure contains very high velocity which somehow contribute to the in-cylinder turbulence. However, information about the degree of turbulence gain and its contribution to improvement of the mixture formation is lacking.
- There have been no investigations of air entrainment with respect to ultra-high pressures, not how the increase in injection pressure support the air entrainment.
- Previous studies have claimed that increased injection pressures improve the fuel-air mixture homogeneity, but that there is no evidence for this at ultra-high pressures.

- The spray penetration length is highly increased by increasing the injection pressure and, subsequently, escalate the chance of the spray hitting the engine walls. None of the previous studies have shown the limitations with respect to the amount of fuel deposited on the engine walls.

This thesis is divided into five sections. In the first chapter, there is a brief introduction, along with the motivation and challenges, and some previous relevant studies of higher fuel injection pressures are presented. Chapter 2 gives a brief description of spray fundamentals. A detailed description of the numerical models is provided in Chapter 3. The governing equations are discussed in detail, followed by the turbulence modeling framework utilized. The spray modeling that was used is explained including the sub-models e.g. injection model, breakup model, dispersion model, evaporation model and droplet-gas interaction. Finally, the spray-wall interaction, including liquid-film modeling, is described. Chapter 4 is divided into two parts relating to the tests using the constant volume spray chamber and the optical engine. In each part, detailed description of the boundary condition, numerical setup and meshing work is mentioned. Then, the important results in terms of droplet atomization, spray-induced turbulence, air entrainment and fuel-air mixture formation are presented and discussed. The limitations with respect to film mass deposition on the engine walls are also highlighted. The conclusions and future scopes of this work are summarized in Chapter 5 and 6, respectively. A brief summary of the published papers is mentioned in Chapter 7.

Chapter 2

Spray Fundamentals

This chapter provides basic fundamental concepts of spray and elaborated in the subsequent chapters. A spray is defined as a dynamic collection of drops dispersed in a gas. A spray is generated by atomization process which can be formed by several methods. The most common method of spray generation is through a nozzle which typically has a fluid passage that is acted upon by different mechanical forces that atomize the liquid. Spray has various applications in different fields including transportation (engines and gas turbines), electrical power generation (lime spray to absorb and remove acid gases from coal-fired power plants), manufacturing (applying adhesive, lubricating bearings, and cooling tools in machining operations, painting), food and beverage (instant coffee, powdered soups, and flavor concentrates), fire protection (water spray), agriculture (herbicides, insecticides, and pesticides spray), and chemical and pharmaceutical (medicine spray). A better understanding of spray formation is important to improve system efficiency depending on area of application. In this work, the application of spray is for engine is used.

2.1 Spray in Engine

In engine application, in particular gasoline engine, fuel is injected either directly into the cylinder or in the intake manifold. An injection of fuel directly into the engine cylinder is known as gasoline direct injection (GDI) engine. In recent years, GDI engine is widely adopted by automotive industry because it can provide higher engine efficiency and power output with lower exhaust emissions than port fuel injection. However, GDI engine tends to produce higher particulate emissions due to imperfect fuel-air mixture formation which remains a major challenge in GDI engine development. For further development of GDI engine, a fundamental understanding of spray formation and spray-turbulence interaction is needed. The

spray characteristics such as better fuel atomization in shortest possible penetration length, refined droplet sizes and better droplet size distribution, plays an important role to enhance engine efficiency. Therefore, it is valuable to determine the spray characteristics quantitatively and qualitatively by experiments and simulations techniques. A large part of thesis related to modeling and simulation of fuel spray to conclude spray characteristics at ultra-high injection pressures.

2.2 Multiphase Flow Modeling

A multiphase flow refers to the simultaneous flow of more than one fluid phase. Here, the discussion is limited to two-phases in the form of gas-liquid flows. Fuel spray consists two phases: dispersed phase (liquid fuel droplets) and continuous phase (surrounding gas). An accurate modeling of spray formation is very important because it governs the fuel-air mixture formation inside the engine. In CFD, several methods have been proposed to model the multiphase system, which are mainly classify as interface resolving approach or non-interface resolving approach.

In the interface resolved method, processes occurring at the interface between continuous and dispersed phases are taken into account. This method can yield a very accurate solution of liquid-gas multiphase system, however, it may be unsuitable for dense sprays due to computational requirements. This method needs a very fine mesh to accurately capture the physics at phases interface. Examples of this method are Volume of Fluid, Two-Fluid method and Immersed Boundary Method.

In the non-interface resolved method, the behavior of group of particles is taken into account and details of the interface are left out. Examples of this method are Lagrangian Particle Tracking (LPT) and Method of Moments. The LPT is most common approach to model sprays in engine. In this approach, dispersed phase is treated as Lagrangian particles and continuous phase is accounted by Eulerian frame, also known as Eulerian-Lagrangian approach. The continuous phase is governed by solving conservation equation for mass, momentum, energy and species. In dispersed phase, each particle represents a collection of droplets, and submodels are applied on droplets to account for physical processes, such as primary and secondary breakup, evaporation, heat and mass transfer, and dispersion. In this work, Eulerian-Lagrangian approach is used to model the spray. The governing equations of continuous phase and all specific submodels applied to droplets are discussed in detail in chapter 3.

2.2.1 Interaction Between the Phases

In multiphase flow, numerical models have to treat the interactions between the different phases. A fuel spray can be dilute or dense depending on the volume fraction of the dispersed particles. A dilute spray can have 1-way or 2-way coupling between the continuous and dispersed phases. In 1-way coupling, only the continuous phase interacts with the dispersed or vice versa such as droplet dispersion due to turbulence. In 2-way coupling, the interaction between the continuous phase and the dispersed phase occurs such as the turbulence causing droplet dispersion and droplet causing mass, momentum, and energy transfer from the liquid to gas. While, a dense spray can also have previously discussed interactions along with the interactions between the particles (i.e. 3-way coupling) such as collision between the droplets. In addition, the dispersed particles can interact with wall i.e. 4-way coupling. A dense spray inside the engine can lead to 4-way coupling.

Chapter 3

Numerical Modeling

This chapter provides an introduction to the mathematical modeling of a fluid and dispersed phase of a multiphase flow. First, the governing equations for a compressible flow are presented and the concept of turbulence is introduced. Then, the spray sub-models and spray-wall interactions are discussed.

3.1 Governing Equations

This section briefly describes a general transport equation for the continuous Eulerian gas phase, which provides the basis for the conservation equations described in the following sections. The governing conservation equations for the flow of continuous media are all specific forms of the same type of balance equation. For a detailed derivation, author refer to the literature [23, 32, 33].

The rate of change of an arbitrary property Φ of a fluid element traveling in an N -dimensional space is described by its total derivative with respect to time t and spatial coordinates x :

$$\frac{D\Phi}{Dt} = \frac{\partial\Phi}{\partial t} + \sum_{i=1}^N \frac{\partial\Phi}{\partial x_i} \frac{\partial x_i}{\partial t}. \quad (3.1)$$

In Eqn. 3.1, the term $D\Phi/Dt$ is the so-called material derivative. The term $\partial x_i/\partial t$ corresponds to the velocity component \mathbf{u}_i in the i^{th} direction, expressed as:

$$\frac{D\Phi}{Dt} = \frac{\partial\Phi}{\partial t} + \sum_{i=1}^N \mathbf{u}_i \frac{\partial\Phi}{\partial x_i}, \quad (3.2)$$

or in vector notation as:

$$\frac{D\Phi}{Dt} = \frac{\partial\Phi}{\partial t} + \mathbf{u} \cdot \nabla\Phi. \quad (3.3)$$

Consider a fixed, time-invariant, non-deformable control volume V with the boundary S . An equivalent Eulerian description of motion of the control volume within a fluid system is obtained by applying Reynold's theorem, as:

$$\frac{d\Phi}{dt} = \frac{d}{dt} \left(\int_V \phi \rho dV \right) + \oint_S \phi \rho \mathbf{u} \cdot \mathbf{n} dS, \quad (3.4)$$

here, ϕ is the intensive property related to the extensive property $\Phi = m\phi$, and \mathbf{n} is the unit normal vector. After applying Leibniz's integral rule:

$$\frac{d}{dt} \int_V f dV = \int_V \frac{\partial f}{\partial t} dV + \oint_S \mathbf{n} \cdot \mathbf{u} f dS, \quad (3.5)$$

Eqn. 3.4 can be written as:

$$\frac{d\Phi}{dt} = \int_V \frac{\partial}{\partial t} \phi \rho dV + \oint_S \phi \rho \mathbf{u} \cdot \mathbf{n} dS. \quad (3.6)$$

Applying Gauss divergent theorem:

$$\int_V \nabla \cdot \mathbf{f} dV = \oint_S \mathbf{n} \cdot \mathbf{f} dS, \quad (3.7)$$

then Eqn. 3.6 can be transformed into a volume integral, and the rate of change is finally given as:

$$\frac{d\Phi}{dt} = \int_V \left[\frac{\partial}{\partial t} \phi \rho + \nabla \cdot (\rho \mathbf{u} \phi) \right] dV. \quad (3.8)$$

Eqn. 3.8 serves as a basis to derive the Eulerian transport equation, obeying the laws of continuum mechanics and thermodynamics with respect to a mass of fixed identity.

3.1.1 Continuity Equation

Consider a fluid element having a control volume V with surface S , as depicted in Fig. 3.1. The principle of conservation of mass states that the mass in a closed system will remain constant, i.e. $dm/dt = 0$. However, in multiphase flow, the mass is exchanged between the phases, which can be accounted for by introducing a source term per unit volume S_ρ , reads as:

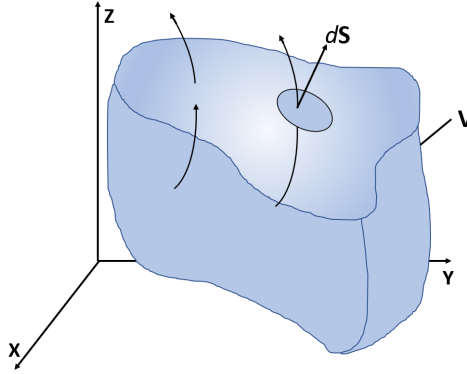


Figure 3.1: Conservation of mass for a fluid element having mass m and volume V with boundary S .

$$\int_V \left(\frac{\partial \rho}{\partial t} + \nabla \cdot \mathbf{u}\rho - S_\rho \right) dV = 0. \quad (3.9)$$

The mass conservation equation for any control volume can be expressed as:

$$\frac{\partial \rho}{\partial t} + \nabla \cdot \mathbf{u}\rho = S_\rho. \quad (3.10)$$

3.1.2 Momentum Equation

Consider a fluid element having mass m , control volume V with surface S and acting forces \mathbf{F} , as shown in Fig. 3.2. The principle of conservation of momentum states that the linear momentum within the control volume is constant. The momentum equation is derived from the conservation of linear momentum and Newton's second law, as:

$$\mathbf{F} = m\mathbf{a} = m \frac{d\mathbf{u}}{dt}. \quad (3.11)$$

Here, \mathbf{F} is the force acting on the system and \mathbf{a} is the acceleration vector. For a constant mass system this is equivalent to:

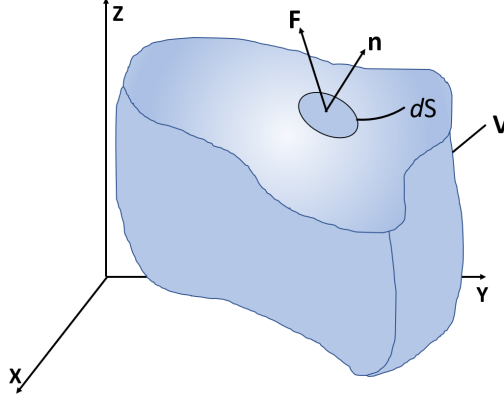


Figure 3.2: Conservation of momentum for a fluid element having mass m , volume V with boundary S and acting forces \mathbf{F} .

$$\frac{d}{dt}(m\mathbf{u}) = \sum \mathbf{F}. \quad (3.12)$$

The forces acting on a fluid element can be divided into body forces (gravitation) and surface force (stresses acting on the fluid surfaces). Then the change of momentum is given by:

$$\frac{d}{dt}(m\mathbf{u}) = \int_V \rho \mathbf{g} dV + \oint_S \boldsymbol{\sigma} \cdot \mathbf{n} dS, \quad (3.13)$$

here, \mathbf{g} is the acceleration due to gravity and $\boldsymbol{\sigma}$ is the stress tensor that can be decomposed into static pressure and viscous stresses, thus:

$$\boldsymbol{\sigma} = -p \mathbf{I} + \boldsymbol{\tau}, \quad (3.14)$$

here p , \mathbf{I} and $\boldsymbol{\tau}$ are the static pressure, the identity tensor and the viscous stress tensor, respectively. Using the stress tensor expression and Gauss divergence theorem, the second term on the RHS of Eqn. 3.13 can be rewritten as:

$$\oint_S \boldsymbol{\sigma} \cdot \mathbf{n} dS = \int_V \nabla \cdot (-p\mathbf{I} + \boldsymbol{\tau}) dV = \int_V (-\nabla p + \nabla \cdot \boldsymbol{\tau}) dV. \quad (3.15)$$

Substituting $\phi = \mathbf{u}$, Eqn. 3.13 and Eqn. 3.15 into the general fluid flow equation yields:

$$\int_V \left(\frac{\partial}{\partial t}(\rho \mathbf{u}) + \nabla \cdot (\rho \mathbf{u} \mathbf{u}) \right) dV = \int_V (-\nabla p + \nabla \cdot \boldsymbol{\tau} + \rho \mathbf{g}) dV. \quad (3.16)$$

After rewriting:

$$\frac{\partial}{\partial t}(\rho \mathbf{u}) + \nabla \cdot (\rho \mathbf{u} \mathbf{u}) = -\nabla p + \nabla \cdot \boldsymbol{\tau} + \rho \mathbf{g}, \quad (3.17)$$

Eqn. 3.17 is the general equation for the conservation of momentum.

3.1.3 Energy Equation

The principle of conservation of energy is governed by the first law of thermodynamics which states that energy can neither be created nor destroyed during a process, it can only change from one form into another. Consequently, the sum of all forms of energy in an isolated system remains constant. The energy conservation equation needs the most attention since many different forms exist. Here, we use the governing equation for the total enthalpy h_t , the sum of the sensible enthalpy h_s and the kinetic energy K , reads:

$$h_t = h_s + K. \quad (3.18)$$

The energy transport equation is the rate of change of the total energy e in a system and is equal to the rate of heat \dot{q} added to the system and the rate of work done \dot{w} on the system, expressed as:

$$\frac{de}{dt} = \dot{q} + \dot{w}. \quad (3.19)$$

The rate of transferred heat is composed of a heat flux rate transferred across the boundaries \dot{q}_s and a source term S_h . Likewise, the rate of work can be divided into the rate of work done by body forces \dot{w}_b and by surface forces \dot{w}_s . Thus, the first law of thermodynamics can be written as:

$$\frac{de}{dt} = \dot{q}_s + S_h + \dot{w}_b + \dot{w}_s. \quad (3.20)$$

By definition, the rate of work can be expressed in terms of force (\mathbf{F}) and velocity (\mathbf{u}), as:

$$\dot{w}_b = \int_V (\mathbf{F}_b \cdot \mathbf{u}) dV,$$

$$\dot{w}_s = \oint_S (\mathbf{F}_s \cdot \mathbf{u}) \cdot \mathbf{n} dS.$$

Applying the Gauss divergence theorem after decomposing the surface forces into pressure p and the viscous force $\boldsymbol{\tau}$, \dot{w}_s becomes:

$$\dot{w}_s = \oint_S (\mathbf{F}_s \cdot \mathbf{u}) \cdot \mathbf{n} dS = \int_V \boldsymbol{\nabla} \cdot (\mathbf{F}_s \cdot \mathbf{u}) dV = \int_V \boldsymbol{\nabla} \cdot [(-p \mathbf{I} + \boldsymbol{\tau}) \cdot \mathbf{u}] dV. \quad (3.21)$$

After manipulation, \dot{w}_s can be rewritten as:

$$\dot{w}_s = \int_V [-\boldsymbol{\nabla} \cdot (p\mathbf{u}) + \boldsymbol{\nabla} \cdot (\boldsymbol{\tau} \cdot \mathbf{u})] dV. \quad (3.22)$$

Applying the Reynolds transport theorem and substituting the rate of work terms with their equivalent expressions, Eqn. 3.8 becomes:

$$\begin{aligned} \int_V \left[\frac{\partial}{\partial t} \rho h_t + \boldsymbol{\nabla} \cdot (\rho h_t \mathbf{u}) \right] dV &= \int_V \boldsymbol{\nabla} \cdot \dot{q}_s dV + S_h + \int_V (\mathbf{F}_b \cdot \mathbf{u}) dV \\ &+ \int_V [-\boldsymbol{\nabla} \cdot (p\mathbf{u}) + \boldsymbol{\nabla} \cdot (\boldsymbol{\tau} \cdot \mathbf{u})] dV. \end{aligned} \quad (3.23)$$

After collecting terms together, the final energy equation for any control volume is:

$$\frac{\partial}{\partial t} \rho h_t + \boldsymbol{\nabla} \cdot (\rho h_t \mathbf{u}) = \boldsymbol{\nabla} \cdot \dot{q}_s + \mathbf{F}_b \cdot \mathbf{u} - \boldsymbol{\nabla} \cdot (p\mathbf{u}) + \boldsymbol{\nabla} \cdot (\boldsymbol{\tau} \cdot \mathbf{u}) + S_h. \quad (3.24)$$

3.1.4 Constitutive Equation

The coupling between the pressure, temperature and density is accounted for by using the ideal gas law derived from the kinetic theory of gases [34], expressed as:

$$p = \rho RT, \quad c_v = \frac{R}{\gamma - 1}, \quad c_p = c_v + R. \quad (3.25)$$

Here, R is the universal gas constant. The specific heat capacity at constant pressure and constant volume is indicated by c_p and c_v , respectively. The dynamic viscosity is obtained by the standard kinetic theory of gas for the Newtonian fluids [35], expressed as:

$$\mu = \frac{A_s \sqrt{T}}{1 + T_s/T}. \quad (3.26)$$

Here, A_s denotes the Sutherland coefficient and T_s the Sutherland temperature.

3.2 Turbulence Modeling

In many engineering applications, the flow can be classified as either laminar, transient or turbulent. The state of the flow can be characterized by the dimensionless Reynolds number Re [36], which is defined as the ratio between inertial forces and viscous forces:

$$Re = \frac{\mathbf{u}L}{\nu}, \quad (3.27)$$

with \mathbf{u} is a characteristic velocity, L the characteristic length, and ν the kinematic viscosity [37]. The characteristic length scale depends on the flow configuration being considered. When the inertial forces are dominant compared to viscous forces e.g. intake air flow inside the combustion chamber, the flow will be a highly chaotic three-dimensional velocity motion. When viscous forces are leading, such as in the flow of honey, the flow is slow and smooth. These two flow states are defined as turbulent and laminar flow, respectively. In industrial problems, the flow is mostly turbulent, particularly in mixing control problems. One of the main reasons is that turbulent flow is a much stronger mixing force than molecular mixing through diffusion.

Within the turbulent flow, different length scales exist. The biggest scale depends on the geometry and the smallest scale depends on the fluid viscosity and the dissipation ϵ . Most of the turbulence energy are coupled with large eddies, which breakup and exchange their energy with smaller eddies. The smaller eddies are further broken down into even more smaller eddies until they are dissipated as heat. This process is known as energy cascade [38]. This energy cascade process ends when the eddies are at their smallest, which is predominately determined by the molecular viscous dissipation. Assuming the largest eddy, having a scale l_I is proportional to \mathbf{u}'^2 (turbulent velocity fluctuations) and an eddy turnover time $t_I = l_I/\mathbf{u}'$, then their ratio will be defined as the dissipation rate ϵ of the smallest scale, as:

$$\epsilon \sim \frac{\mathbf{u}^3}{l_I}. \quad (3.28)$$

The dissipation energy of smaller eddies allow the estimation of the smallest length scales l_η (also known as Kolmogorov length scale) and time scale τ_η , as:

$$l_\eta = \left(\frac{\nu^3}{\epsilon} \right)^{1/4}, \quad (3.29)$$

$$\tau_\eta = \left(\frac{\nu}{\epsilon} \right)^{1/2}. \quad (3.30)$$

The biggest length scale l_I (also known as the integral length scale) is calculated by estimating the auto-correlation coefficients (under certain assumptions) at two points in the flow with variable distance between them. The normalized auto-correlation coefficient R_x is then:

$$R_x(r) = \frac{\mathbf{u}'(x) \mathbf{u}'(x+r)}{\mathbf{u}'(x)^2}, \quad (3.31)$$

here, r is the distance between two points in the flow. The integration of the auto-correlation curves results in the integral length scale:

$$l_I = \int_0^\infty R_x dr. \quad (3.32)$$

Energy Spectrum

The turbulent kinetic energy spectrum E_κ in wave number space $\kappa = 2\pi/l$ can be evaluated using a Fourier Transformation of the auto-correlation coefficient. A schematic plot of turbulent kinetic energy is shown in Fig. 3.3, with the maximum energy at the integral length scale and the minimum energy at the Kolmogorov scale. The energy transfer from bigger to smaller eddies occurs within the inertial subrange with a decay curve following the $\kappa^{-5/3}$ law [39]. More detailed information about the turbulent energy spectrum can found in [39].

Strategies to Model Turbulent Flow

In CFD, there are many well-established fundamental methods for modeling turbulent flow, all with their own strengths and weaknesses. Direct Numerical Simulation

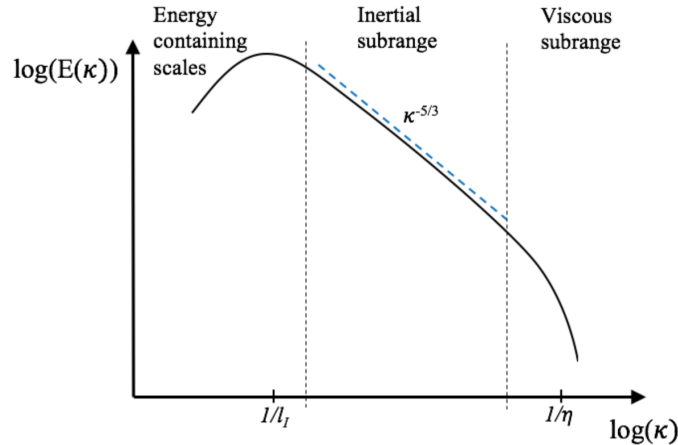


Figure 3.3: Schematic of energy spectrum of decay of isotropic homogeneous turbulence [40].

(DNS), has the potential to resolve the whole spectrum of motion from large energy-carrying eddies down to the Kolmogorov scale. In this method, a spatial discretization of the order of the Kolmogorov scale is needed. An estimation of the required grid size can be calculated by:

$$N_{DNS} = \left(\frac{L}{l_\eta}\right)^3 Re_t^{-9/4}. \quad (3.33)$$

DNS is the most accurate method, however, computationally very expensive. DNS is only practical for low Reynolds number cases and mainly serves as a tool for fundamental research. A DNS application to the in-cylinder flow and spray has so far not been reported, only an engine like geometry with relatively low engine speed has been performed [41].

Second, Reynolds averaged Navier-Stokes (RANS) is an approach in which the whole energy spectrum is modeled. In this approach, the Reynolds decomposition and a temporal averaging is applied to the governing equations. The averaging procedure obviously loses some information contained in the instantaneous equations. The Reynolds decomposition results in a new unclosed term known as the Reynolds stress tensor. The unclosed Reynolds stress tensor can be handled using different procedures leading to different RANS turbulence models. The main limitation of the RANS approach is that it provides the mean information while details about the instantaneous processes, such as cyclic variability, are lost. A refinement of the grid or time-step marginally improves the numerical accuracy but does not

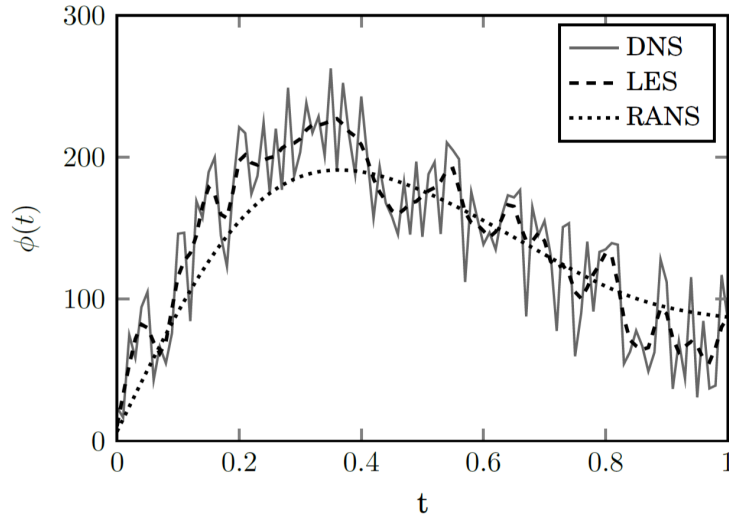


Figure 3.4: Comparison of a quantitative solution obtained from DNS, LES and RANS simulations.

inherently increase the range of scales resolved. Moreover, modeling the effects of all scales of motion is challenging. In many industrial applications, RANS is still widely used, even though it only offers the time-averaged results, because of its lower computational cost. In its application to reciprocating engines, an unsteady-RANS (URANS) has been successfully applied to calculate the ensemble mean values and was able to capture the dynamic behaviour to some extent. However, it failed to calculate all of the cyclic variations simply because they were not included in the model. This method also requires some effort for the identification of the model parameters and their validation; these parameters are only valid for a particular engine. The URANS approach could be interpreted as a very coarse Large-Eddy Simulation.

The third approach, Large-Eddy Simulation (LES), can potentially provide more detailed information (compared to RANS/URANS) by directly resolving large turbulent scales and modeling small (universal) turbulent scales. This method is less computational demanding than DNS and more accurate than RANS, with the capability to resolve time-dependent events. A schematic comparison between all three methods is shown in Fig. 3.4. The LES approach is used in the scope of this thesis.

3.2.1 Large Eddy Simulation

Large-Eddy Simulation is a multi-scale technique with an accuracy stands between the DNS and RANS approaches. The fundamental idea of LES is to resolve the large energy containing eddies directly and to model the small-scale turbulent structures. The instantaneous flow field can be split into the resolved part ($\tilde{\phi}$) and the unresolved/modeled part (ϕ^{sgs}), expressed as:

$$\phi = \tilde{\phi} + \phi^{sgs}. \quad (3.34)$$

Now, the extraction of the resolved large-scale part from the variable ϕ is achieved by a convolution of the variable with a filter kernel G , as:

$$\tilde{\phi}(x_i) = \int_V \phi(x_i^*) G(x_i, x_i^*, \Delta) dx_i^*. \quad (3.35)$$

Here, the tilde denotes LES filtered quantities. The filtering operation removes all finer fluctuations and the governing equations only describe the space-filtered fields. There are many expressions for filter function are exist. The author recommends to follow Pope et. al. [39] for a detailed description of filtering operations.

In the scope of this thesis, no filter function was applied explicitly. The filtering operation was implicitly taken into account by the LES grid, where the filter width was estimated using the cubic root of the local computational cell volume ΔV , as:

$$\Delta = \sqrt[3]{\Delta V}. \quad (3.36)$$

Filtered Governing Equations

For compressible flows with large density change, it is convenient to use Favre-filtering [42] or density-weighted filtering, expressed as:

$$\tilde{\phi} = \frac{\overline{\rho\phi}}{\bar{\rho}}. \quad (3.37)$$

Here, an overline denotes conventional and a tilde represents Favre-filtered quantities. Now, the conservation equations for mass, momentum and energy are expressed after Favre-averaging as:

$$\frac{\partial \bar{p}}{\partial t} + \frac{\partial(\bar{\rho} \tilde{\mathbf{u}}_j)}{\partial x_j} = \tilde{S}_\rho, \quad (3.38)$$

$$\frac{\partial(\bar{\rho} \tilde{\mathbf{u}}_i)}{\partial t} + \frac{\partial(\bar{\rho} \tilde{\mathbf{u}}_i \tilde{\mathbf{u}}_j)}{\partial x_j} = \frac{\partial \bar{\tau}_{ij}}{\partial x_j} + \frac{\partial \boldsymbol{\tau}_{ij}^{sgs}}{\partial x_j} - \frac{\partial \bar{p}}{\partial x_i} + \tilde{S}_{u,i}, \quad (3.39)$$

$$\frac{\partial(\bar{\rho} \tilde{h}_t)}{\partial t} + \frac{\partial(\bar{\rho} \tilde{h}_t \tilde{\mathbf{u}}_j)}{\partial x_j} = \frac{\partial}{\partial x_j} \left(\alpha_{eff} \frac{\partial \tilde{h}_t}{\partial x_j} \right) + \frac{\partial \bar{p}}{\partial t} + (\bar{\tau}_{ij} + \boldsymbol{\tau}_{ij}^{sgs}) \frac{\partial \tilde{\mathbf{u}}_i}{\partial x_j} + \tilde{S}_h. \quad (3.40)$$

In the governing equations, ρ is the density, \mathbf{u}_j the flow velocity vector, p the pressure, $\boldsymbol{\tau}_{ij}$ the viscous shear stress tensor, α_{eff} the thermal diffusivity, and h_t the total enthalpy $h_t = h_s + (\mathbf{u}_j \mathbf{u}_j)/2$ where h_s denotes sensible enthalpy. S_ρ , $S_{u,i}$ and S_h are respectively the mass, momentum and energy source terms from the dispersed phase accounting for the coupling between the liquid and gas phases. The pressure was calculated using pressure-velocity-density coupling for flows with an arbitrary Mach number [43]. The molecular viscosity was calculated using Sutherland law [35], as described by Eqn. 3.26. Note that, after the Favre-filtering operation on the momentum equation, an unresolved sub-grid stress tensor $\boldsymbol{\tau}^{sgs}$ appears.

Sub-grid Stress Modeling

The filtering operation of the governing equations result in an additional sub-grid scale (SGS) term that needs to be closed. The SGS term represents the interactions between the resolved and unresolved parts of the flow [44]. According to the Boussinesq hypothesis, the unresolved Reynolds stress tensor can be modeled using turbulent eddy viscosity ν_t , expressed as:

$$\boldsymbol{\tau}_{ij} - \frac{1}{3} \delta_{ij} \boldsymbol{\tau}_{kk} = -\mu_t \left(\frac{\partial \tilde{\mathbf{u}}_i}{\partial x_j} + \frac{\partial \tilde{\mathbf{u}}_j}{\partial x_i} - \frac{2}{3} \delta_{ij} \frac{\partial \tilde{\mathbf{u}}_k}{\partial x_k} \right) = -2\mu_{sgs} \left(\tilde{\mathbf{S}}_{ij} - \frac{1}{3} \tilde{\mathbf{S}}_{kk} \delta_{ij} \right). \quad (3.41)$$

The eddy viscosity can be modeled using an algebraic expression or with the transport equation for turbulent kinetic energy. In this work, the standard Smagorinsky model [45] was used, in which the turbulent viscosity is calculated as:

$$\mu_{sgs} = \rho \nu_{sgs} = \rho C_k \Delta \sqrt{k_{sgs}}. \quad (3.42)$$

Here, C_k is a model constant and k_{sgs} is the sub-grid scale kinetic energy. The sub-grid scale turbulence can be modeled as:

$$k_{sgs} = \frac{2C_k}{C_\epsilon} \Delta^2 \tilde{\mathbf{S}}^2, \quad (3.43)$$

here, C_ϵ is another model constant. The resolved shear stress $\tilde{\mathbf{S}}$ can be defined as:

$$\tilde{\mathbf{S}} = 2 \sqrt{\tilde{\mathbf{S}}_{ij} \tilde{\mathbf{S}}_{ij}} \quad \text{with} \quad \tilde{\mathbf{S}}_{ij} = \frac{1}{2} \left(\frac{\partial \tilde{\mathbf{u}}_i}{\partial x_j} + \frac{\partial \tilde{\mathbf{u}}_j}{\partial x_i} \right). \quad (3.44)$$

The final expression of the turbulent viscosity in the standard Smagorinsky model [45] is defined as:

$$\nu_{sgs} = \left(\sqrt{\frac{2 C_k^{1.5}}{C_\epsilon^{0.5}} \Delta} \right)^2 \sqrt{2 \tilde{\mathbf{S}}_{ij} \tilde{\mathbf{S}}_{ij}} \quad \text{or}, \quad (3.45)$$

$$\nu_{sgs} = C_S^2 \sqrt{2 \tilde{\mathbf{S}}_{ij} \tilde{\mathbf{S}}_{ij}} \quad \text{with} \quad C_S = \left(\sqrt{\frac{2 C_k^{1.5}}{C_\epsilon^{0.5}} \Delta} \right). \quad (3.46)$$

The Smagorinsky model constant C_S is typically set to 0.2 [46] for homogeneous isotropic turbulence.

3.3 Spray Modeling

3.3.1 Liquid Injection Model

In this work, a blob injection model was used in combination with the Kelvin-Helmholtz Rayleigh-Taylor (KH-RT) breakup model, as shown in Fig. 3.5. In the blob injection method [47], a set of parcels representing blobs or portions of the injected liquid column is injected into the computational domain within a prescribed spray-cone angle. Each blob is characterized by an initial diameter d_{inj} , which is equal to, or less than, the effective nozzle orifice diameter d_{noz} . The injected diameter and velocity of each injected blob is calculated as:

$$d_{inj} = \sqrt{c_d} d_{noz}, \quad (3.47)$$

$$\mathbf{u}_{inj} = \frac{\dot{m}}{\rho_p A c_d}. \quad (3.48)$$

Here, c_d denotes the nozzle discharge coefficient, A is the nozzle orifice cross-sectional area and \dot{m} is the mass flow rate. The detailed simulation of near-nozzle phenomena is replaced by the injection of big spherical droplets. In this work, the number of droplets injected per unit time was calculated based on the measured mass flow rate profile (see Appendix).

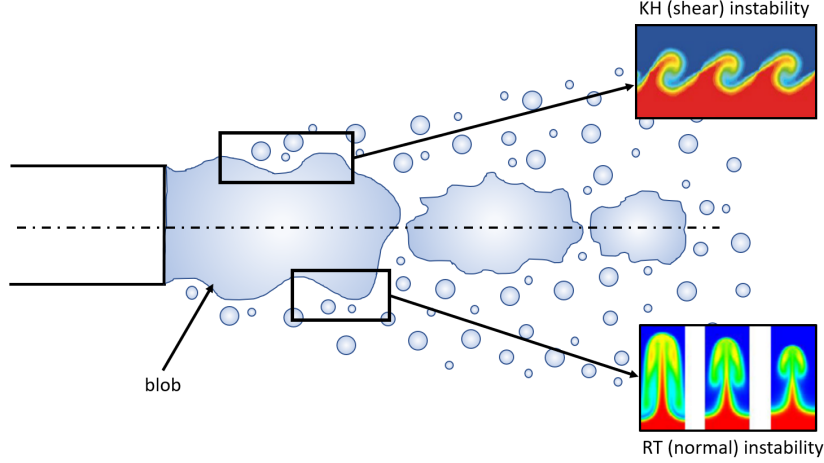


Figure 3.5: Atomization mechanism using the Kelvin–Helmholtz/Rayleigh–Taylor (KH–RT) instability model.

3.3.2 Droplet Motion

A real spray contains very large number of droplets, and solving the equations of motion for each droplet would be computationally expensive. Therefore, multiple droplets with identical properties are grouped together into a single term ‘parcel’. In parcel approach, each parcel represents an average droplet/particle at a given point and, therefore, this approach can handle very large number of droplets with reasonable computational power.

In the simulation, liquid fuel parcels are injected at very high injection pressures into a quiescent or turbulent environment. The liquid parcels then start to be decelerated by interactions (drag) with the gas phase. This results in an exchange of momentum between the gas and liquid phases, mainly due to their different relative velocities. This exchange of momentum is evaluated by assuming that the drag force acting on a liquid parcel, as:

$$\frac{1}{6}\rho_p\pi d^3\frac{d\mathbf{u}_p}{dt} = \frac{1}{2}(\mathbf{u}_g - \mathbf{u}_p)|\mathbf{u}_g - \mathbf{u}_p|\rho_g C_D \frac{\pi d^2}{4}, \quad (3.49)$$

here, d is the droplet diameter, ρ_p the particle density, \mathbf{u}_p the particle velocity, and ρ_g the gas density. The gas velocity \mathbf{u}_g is interpolated to the particle position from the adjacent cells, and C_D is the coefficient of drag force acting on a droplet, defined as:

$$C_D = \frac{24}{Re_p} \left(1 + \frac{1}{6} Re_p^{2/3} \right) \text{ for } Re_p < 1000, \quad (3.50)$$

$$C_D = 0.424 \quad \text{for } Re_p > 1000. \quad (3.51)$$

The Reynolds number of the particle is calculated using the viscosity of the gas ν_g , as:

$$Re_p = \frac{|\mathbf{u}_g - \mathbf{u}_p|d}{\nu_g}. \quad (3.52)$$

The position of parcels \mathbf{x}_p with respect to time t is given by $d\mathbf{x}_p/dt = \mathbf{u}_p$.

3.3.3 Secondary Droplet Breakup Model

Spray atomization can be divided into two main steps: primary breakup of the liquid jet and secondary breakup into droplets and ligaments. In this work, primary breakup was described using the blob method [48], in which blobs of diameter equivalent to the nozzle diameter (see Eqn. 3.47) are injected and the number of droplets injected per unit time is calculated based on a predicted mass flow rate profile. In this way, a detailed simulation of near-nozzle phenomena is replaced by the injection of large spherical droplets that breakup into smaller droplets during secondary breakup. A schematic of the blob injection method is shown in Fig. 3.6.

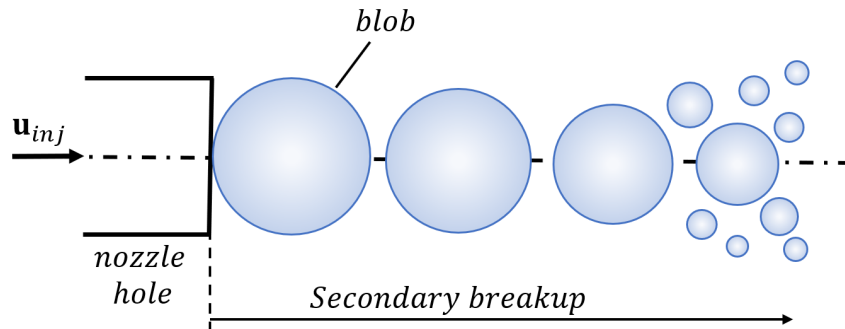


Figure 3.6: Schematics of the blob injection method.

For the secondary breakup, the well-known Kelvin-Helmholtz Rayleigh-Taylor (KH-RT) model [49, 50] was chosen based on the fact that a spray at high injection pressure lies in a breakup regime of a high Weber number. This model combines both Kelvin-Helmholtz (KH) and Rayleigh-Taylor (RT) instabilities. A schematic of the KH and RT breakup is shown in Fig. 3.7.

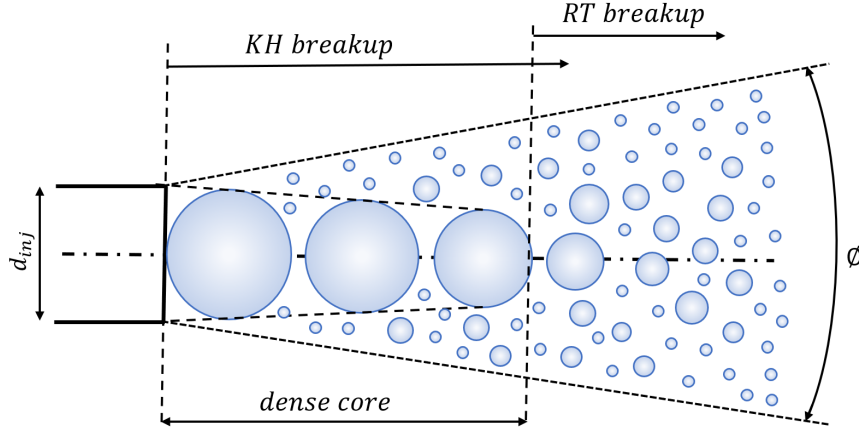


Figure 3.7: Schematics of the KH and RT breakup.

In KH instability, the breakup of fuel injected at higher velocities is independent of the initial radius of the liquid jet, and the unstable growth of perturbations at the liquid-gas interface is attributed to shearing between the fluids. The breakup is calculated based on the wavelength of the fastest growing instabilities due to aerodynamic forces. The fastest growing wave Λ_{KH} and growth rate Ω_{KH} are expressed as:

$$\Lambda_{KH} = 9.02 \frac{r_d(1 + 0.45 Oh^{1/2})(1 + 0.4 Ta^{0.7})}{1 + 0.865 We^{1.67}}, \quad (3.53)$$

$$\Omega_{KH} = \frac{(0.34 + 0.38 We^{3/2})}{(1 + Oh)(1 + 1.4 Ta^{0.6})} \sqrt{\frac{\sigma}{\rho_d r_d^3}}. \quad (3.54)$$

Here, $We = \rho_g |\mathbf{u}_d - \mathbf{u}_g|^2 r_d / \sigma$ is the Weber number, $Oh = \sqrt{We} / Re$ is the Ohnesorge number, $Ta = Oh \sqrt{We}$ is the Taylor number, r_d is the droplet radius, \mathbf{u}_d is the droplet velocity, and σ is the surface tension of liquid droplet. After the KH breakup, the critical droplet radius r_{crit} is the size of new droplets, which is assumed proportional to the wavelength of the fastest growing or most probable unstable surface wave Λ_{KH} , such that:

$$r_{crit} = B_0 \Lambda_{KH}, \quad (3.55)$$

here B_0 is a breakup constant. The breakup time τ_{KH} controls the breakup rate and is a function of the growth rate Ω_{KH} and the fastest growing wave Λ_{KH} , such as:

$$\tau_{KH} = \frac{3.76 B_1 r_d}{\Lambda_{KH} \Omega_{KH}}, \quad (3.56)$$

here B_1 is a breakup constant. The change of radius of the original droplets can be calculated using the following expression:

$$\frac{dr_d}{dt} = -\frac{r_d - r_{crit}}{\tau_{KH}}. \quad (3.57)$$

Rayleigh-Taylor instability waves originate from acceleration normal to the droplet-gas interface on the surface of droplet. The RT breakup occurs when the fluid is accelerated in a direction different to that of the density gradient. When liquid ligaments are decelerated by drag in the gas phase, instability may grow on the trailing edge of the droplet. Therefore, RT breakup is controlled by the rate of disturbance growth on the surface of the droplet. The fastest growing wave Ω_{RT} and wavelength Λ_{RT} are given by:

$$\Omega_{RT} = \sqrt{\frac{2 |\mathbf{g}_t(\rho_l - \rho_g)|^{1.5}}{3\sqrt{3\sigma} (\rho_l - \rho_g)}}, \quad \text{with} \quad (3.58)$$

$$\mathbf{g}_t = \left(\mathbf{g} - \frac{d\mathbf{u}_d}{dt}\right) \cdot \frac{\mathbf{u}_d}{|\mathbf{u}_d|},$$

$$\Lambda_{RT} = 2\pi c_0 \sqrt{\frac{3\sigma}{|\mathbf{g}_t(\rho_l - \rho_g)|}}. \quad (3.59)$$

Here, \mathbf{g} is the gravitational force and c_0 is a modeling parameter. Two criteria determine the outcome of RT breakup: if the wavelength of the fastest growing wave is smaller than the droplet diameter and perturbations are allowed to grow for some time, then the droplet will be replaced by a parcel of smaller droplets when the growth time exceeds the typical RT time. The RT breakup time is given by:

$$\tau_{RT} = \Omega_{RT}^{-1}. \quad (3.60)$$

For KH breakup, the stripped mass of parcels will be allocated to form a new parcel (with a radius of r_{crit}) when the total stripped mass exceeds some proportion of the original mass of parcel. For RT breakup, the number of parcels will be unchanged, but the post-breakup parcels will contain more and smaller identical droplets.

In the simulations, droplet breakup occurs through the mechanism that predicts the shortest breakup time. The Kelvin-Helmholtz mechanism usually dominates near the nozzle exit, while the Rayleigh-Taylor mechanism becomes dominant further downstream. The model is described in more detail elsewhere [51].

3.3.4 Stochastic Droplet Dispersion Model

Turbulent dispersion of droplets was modeled using a stochastic approach suggested by Gosman and Ioannides [52]. The model samples a (non-resolved) sub-grid scale velocity \mathbf{u}^{sgs} from a Gaussian distribution with zero mean and standard deviation $\sqrt{2k_{sgs}/3}$. This is added to the interpolated resolved/filtered gas phase velocity at the droplet location to produce the instantaneous gas phase velocity, as:

$$\mathbf{u}_g = \tilde{\mathbf{u}} + \mathbf{u}^{sgs}. \quad (3.61)$$

The interaction time t_{int} of the droplet with this instantaneous velocity is defined as the minimum of a characteristic eddy turnover time $t_e = l_e/|\mathbf{u}^{sgs}|$ and the transit time t_{tr} needed by the droplet to cross the eddy:

$$t_{int} = \min(t_e, t_{tr}). \quad (3.62)$$

Here, t_e is calculated from the sub-grid scale kinetic energy k_{sgs} and the sub-grid scale dissipation rate ϵ_{sgs} using $t_e = C(k_{sgs}^{3/2}/\epsilon_{sgs})$ with constant $C = 0.1643$. The sub-grid scale kinetic energy is calculated as $k_{sgs} = (\widetilde{\mathbf{u}_i \mathbf{u}_i} - \tilde{\mathbf{u}}_i \tilde{\mathbf{u}}_i)/2$ and the sub-grid scale dissipation rate is evaluated from $\epsilon_{sgs} = k_{sgs}^{3/2}/\Delta$, where Δ denotes the filter size. The eddy transit time is estimated from a linearized form of the equation of motion of the droplet. For further details author refer to [52].

3.3.5 Droplet Evaporation Model

The evaporation of a liquid droplet was modeled using the energy balance on the droplet surface due to heat transfer from the surroundings and latent heat of evaporation (as illustrated in Fig. 3.8), expressed as:

$$Q = \dot{m}_f L + \dot{Q}_i, \quad (3.63)$$

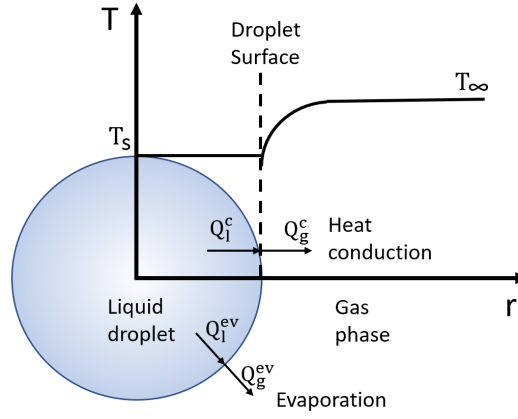


Figure 3.8: Illustration of evaporation process.

here L is the latent heat of liquid droplet. The heat conduction rate \dot{Q}_i from droplet surface into droplet interior is defined as:

$$\dot{Q}_i = 4\pi r^2 h_c (T_\infty - T_s), \quad (3.64)$$

here r is the radius of droplet, and T_∞ and T_s are the ambient and droplet surface temperature, respectively. The Nusselt number based on heat transfer coefficient h_c is calculated as:

$$N_u = \left(2 + 0.6R_e^{1/2}P_r^{1/3}\right) \frac{\ln(1 + B_T)}{B_T}. \quad (3.65)$$

Here, $R_e = 2\rho_g U_r / \mu_g$ denotes the droplet's Reynolds number, Prandtl number is given by $P_r = \mu_g C_p / K_g$ and Spalding heat transfer number is given by $B_T = C_p (T_\infty - T_s) / L_{eff}$. The mass transfer from the droplet using a correlation suggested by Frössling [53] is given by:

$$\dot{m}_f = 2\pi r (\rho D)_g B_m Sh_d, \quad (3.66)$$

where $(\rho D)_g$ is the vapor diffusivity in the air, and the Sherwood number Sh_d is calculated as:

$$Sh_d = \left(2 + 0.6R_e^{1/2}S_c^{1/3}\right) \frac{\ln(1 + B_m)}{B_m}, \quad (3.67)$$

here S_c is the Schmidt number and B_m is the Spalding mass transfer number. More details about the evaporation model can be found in [54].

3.3.6 Droplet Tracking Model

The Eulerian-Lagrangian coupling approach is a commonly method for modeling the spray evolution and mixture formation in an engine. In this approach, fuel injection is represented by discrete Lagrangian parcels which enable a simple implementation. One parcel can represent an arbitrary number of droplets modeled using the mass, diameter, temperature and other characteristic droplet properties. To understand the working principle of this model, consider a particle positioned at point 'a' moving to point 'b', as illustrated in Fig. 3.9.

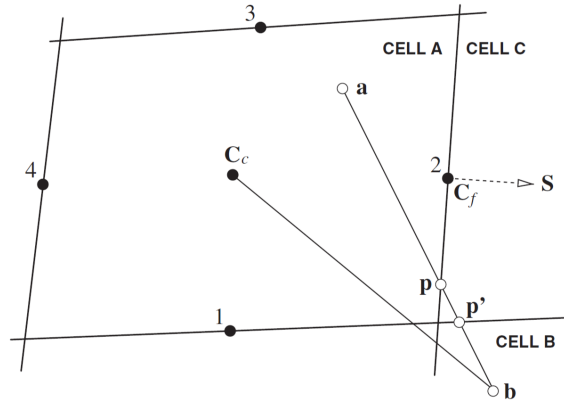


Figure 3.9: Motion of a particle with cell face crossings [55].

The trajectory of the particle is such that it intersects two cells on its way to the final destination at point 'b'. Now, when a particle reaches the boundary of any cell then it needs to be treated separately. The distance from point 'a' and point 'p' is calculated by:

$$d(\mathbf{a}, \mathbf{p}) = \mathbf{a} + \lambda_a(\mathbf{b} - \mathbf{a}). \quad (3.68)$$

Every face of a grid cell can be used to evaluate a location of the particle on that face using face center ‘ C_f ’ along a normal vector ‘ \mathbf{S} ’.

$$(d(\mathbf{a}, \mathbf{p}) - C_f) \cdot \mathbf{S} = 0. \quad (3.69)$$

Substituting the value of $d(\mathbf{a}, \mathbf{p})$, we obtain the value of λ_a , as:

$$\lambda_a = \frac{(C_f - \mathbf{a}) \cdot \mathbf{S}}{(\mathbf{b} - \mathbf{a}) \cdot \mathbf{S}}. \quad (3.70)$$

The Eqn. 3.70 can be used to calculate the value of λ_a for each face of the cell which the particle currently occupies, using each face’s own C_f and \mathbf{S} vector values. The face that the particle will actually cross has the lowest value of λ_a in the interval $0 \leq \lambda_a \leq 1$. More detailed information about the model can be found in [55].

3.4 Spray-Wall Interaction

The interaction between spray parcels and wall surfaces results in a wall-film. The wall-film was modeled using the Bai and Gosman approach [56, 57] as it has been widely validated [58, 59, 60]. The impingement of spray droplets onto a wet surface in that model results in four different regimes: stick, rebounding, spreading and splashing, as illustrated in Fig. 3.10. In the stick regime, the spray droplets hitting the wall are assumed to combine to form a local liquid-film. In the rebound regime, the droplet reflects (without breakup) off the wall but loses a small part of its kinetic energy through deformation of the liquid-film. In the spread regime, all of the droplets hitting the wall become part of the film. In the splash regime, some of the incident droplets are transferred to the wall-film and the remainder rebounded. The splashing process is modeled by introducing three new parcels in the mesh for each droplet colliding with the wall.

The droplet’s Weber number and the Laplace impact number characterize the impingement regimes and are used to identify the regime of spray impingement. The Weber number is defined as the ratio of droplet’s kinetic energy and surface tension:

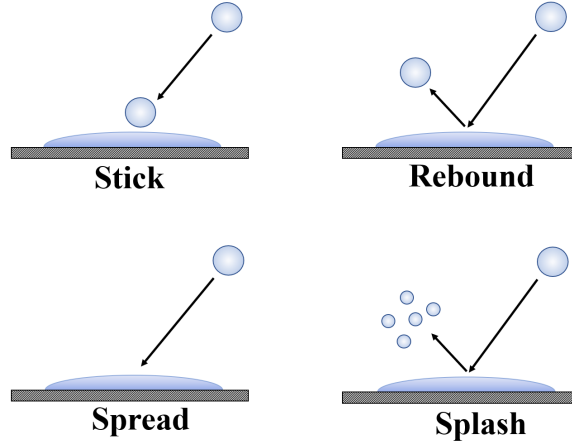


Figure 3.10: Impingement regimes identified in the wall-film impingement model.

$$We = \frac{\rho_l v_n^2 d}{\sigma}, \quad (3.71)$$

and the Laplace impact number is the ratio of droplet surface tension and viscous forces acting on the liquid:

$$L = \frac{\rho_l \sigma d}{\mu_l^2}. \quad (3.72)$$

Here, v_n is droplet velocity, ρ_l the liquid density, σ the surface tension of liquid, and μ_l the dynamic viscosity of liquid.

For a dry wall, the transition between the stick and splash regimes is given by:

$$\text{Stick to Splash: } We_{crit} = 1320La^{-0.18}$$

For a wetted wall, the transition between the regimes is given by:

$$\text{Rebound to Spread: } We_{crit} \approx 5$$

$$\text{Spread to Splash: } We_{crit} = 1320La^{-0.18}$$

A detailed description of the correlations used for momentum and mass exchange between the droplets and the liquid-film in the rebound and splash regimes can be found in [56, 57].

3.4.1 Liquid-film Modeling

The evolution of the resulting liquid-film on a plane surface S_w is illustrated in Fig. 3.11. The film has a free surface S_{fs} with variable thickness δ , having the normal \mathbf{n} and assumed velocity profile \mathbf{v} (varying from zero at the wall to the free surface velocity \mathbf{v}_{fs}). A number of assumptions need to be considered to derive the governing equation of the liquid-film. These include: the film is thin enough for the boundary layer approximation; the film motion occurs through spatial variation in the tangential directions of the local liquid pressure p_L ; shear is produced at the interface between wall and film; a tangential momentum source is generated by impinging droplets and body forces (gravity).

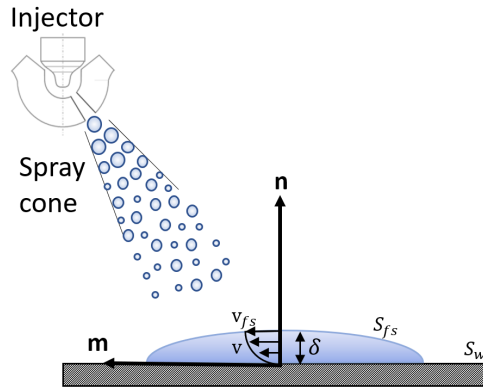


Figure 3.11: Illustration of liquid-film formation following spray impingement.

The continuity equation, assuming incompressibility of the liquid-film, is solved for its local height δ , as:

$$\int_{S_w} \frac{\partial \delta}{\partial t} dS + \oint_{\partial S_w} \delta \mathbf{m} \cdot \bar{\mathbf{v}} dL = \frac{\dot{m}_s}{S_w \rho_L} + \frac{S_{v,d}}{\rho_L}. \quad (3.73)$$

Here, $\bar{\mathbf{v}}$ is the height average liquid-film velocity tangential to the surface S_w , \mathbf{m} is the tangential vector to the wall surface, ρ_L is the liquid-film density, \dot{m}_s is the mass source surface density, and S_v is the mass evaporating from the liquid-film due to dynamic or thermal effects. The evaporating mass due to the dynamic effects is calculated by:

$$S_{v,d} = \frac{\tau_S}{|\mathbf{U}_\infty - \mathbf{U}_f|} [(B_M + 1)^{(1/S_c)} - 1], \quad (3.74)$$

here, τ_S is the liquid shear stress, $\mathbf{U}_\infty - \mathbf{U}_f$ is the relative liquid-gas velocity, and B_M and S_c are the Spalding mass diffusion and Schmidt number, respectively. When thermal effects are dominant, the evaporating mass is estimated by:

$$S_{v,d} = \frac{J_S}{c_{pg} |T_\infty - T_f|} [(B_M + 1)^{(1/L_e)} - 1], \quad (3.75)$$

here, $T_\infty - T_f$ is the temperature difference between the gas and the liquid-film, c_{pg} is the gas specific heat and L_e is the Lewis number.

The momentum equation is solved by considering the liquid-film velocity $\bar{\mathbf{v}}$, as:

$$\begin{aligned} \frac{d}{dt} \int_{S_w} \delta \bar{\mathbf{v}} dS + \oint_{\partial S_w} \mathbf{m} \cdot (\delta \bar{\mathbf{v}} \bar{\mathbf{v}} + \mathbf{C}) dL = & \frac{1}{\rho_L} \int_{S_{fs}=S_w} \tau_{fs} dS - \frac{1}{\rho_L} \int_{S_w} \tau_w dS + \\ & \int_{S_w} \delta \mathbf{g}_t dS - \frac{1}{\rho_L} \int_{S_w} \delta \nabla_s p_L dS + \frac{1}{\rho_L} \int_{S_w} \bar{S}_v dS. \end{aligned} \quad (3.76)$$

Here, τ_{fs} and τ_w are the tangential viscous stresses on the film surface and on the wall, respectively. \mathbf{C} is a correction tensor, \mathbf{g}_t is the acceleration due to gravity in tangential direction, $\nabla_s p_L$ is the surface gradient of the pressure, and \bar{S}_v is the tangential component of the momentum source from impinging droplets.

The enthalpy equation is solved by considering the liquid-film enthalpy h_f as:

$$\frac{d}{dt} \int_{S_w} h_f dS + \oint_{\partial S_w} h_f \mathbf{m} \cdot \bar{\mathbf{v}} dL = J_g - J_w + S_{hf}. \quad (3.77)$$

Here, J_g and J_w are the heat fluxes from the gas and the wall, respectively, and S_{hf} is the source term due to impinging droplets.

The governing equations of liquid-film mass (Eqn. 3.73), momentum (Eqn. 3.76) and energy (Eqn. 3.77) comprise the effects of spray impingement and film evaporation. The governing equations are solved using a segregated solution procedure for the amount of evaporated film mass and corresponding energy transferred to the gas phase. The equations were discretized on the (two-dimensional) wall surfaces (here, piston and liner) of the three-dimensional domain using the Finite Area Method. The liquid-film evolution model allows the interactions between the gas, spray and liquid-

film which are very important for GDI engine simulations since the fuel-air mixing process is affected by in-cylinder flows, spray evolution, and liquid-film dynamics.

3.5 Numerical Solution Algorithm

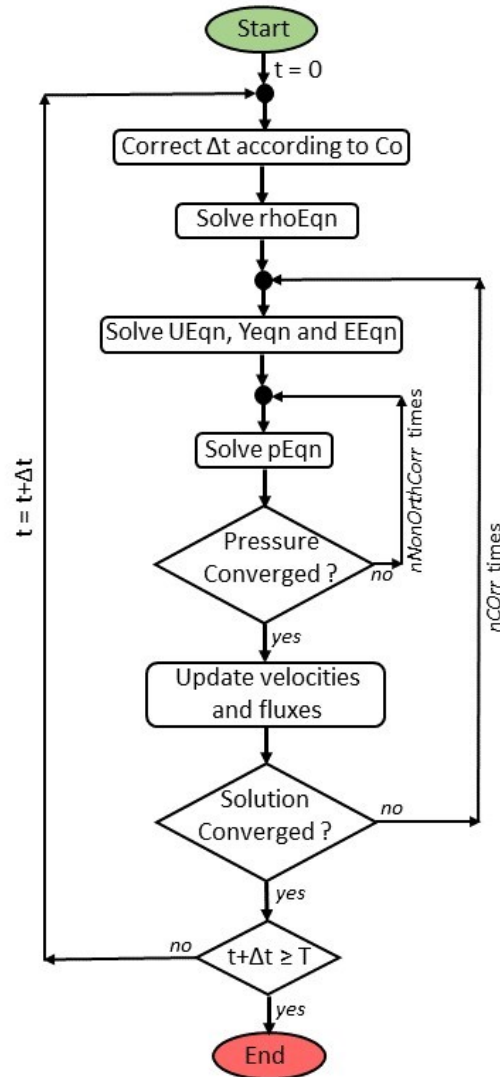


Figure 3.12: Flow chart of the numerical solution algorithm.

The flow chart of the numerical solution algorithm of the flow solver used for the simulations in this work is shown in Fig. 3.12. The pressure-velocity coupling to solve the non-linear Navier-Stokes equations follows the standard PIMPLE (merged PISO-SIMPLE) algorithm. The PIMPLE algorithm provides better stability than the standard PISO algorithm.

Before the PIMPLE loop starts, the density equation (rhoEqn) is solved and the mass fluxes are updated after the pressure convergence. The momentum (UEqn), species (YEqn), and energy equation (EEqn) are solved for velocity, species, and enthalpy, respectively. The PISO loop begins by solving the pressure Poisson equation (pEqn) in an iterative manner to account for non-orthogonal grid effects. Once the pressure equation is solved, the mass fluxes are updated and the velocity is corrected based on the new pressure gradient. The PIMPLE loop starts by solving the momentum equation and other equations and ends after the solution is converged.

For the spray chamber case the numerical solution algorithm follows the scheme as described in the flow chart. However, for the engine cases some changes are required. The equation for the mesh motion is solved followed by an update the fluxes before solving the density equation (rhoEqn).

Chapter 4

Results and Discussion

In this chapter, a summary of results is presented for two test cases: a constant volume spray chamber and an optical GDI engine. In the first test case, a simplified geometry was used to investigate the spray characteristics and behavior at ultra-high injection pressures. The knowledge gained from the spray chamber test case was then applied to the second test case, the optical GDI engine. In the second test case, the main focus was on the fuel-air mixture homogeneity, and the spray-wall interactions: the fuel mass deposition and fuel film evolution, to address the main research questions.

4.1 Constant Volume Spray Chamber

For this test, fuel was injected into a quiescent constant volume spray chamber at selected injection pressures (200, 600, 1000 and 1500 bar). Two different injector nozzles were used. The results compared well with the available experimental data (refer to Paper 2 for the experimental configuration). The main aim of this part of the study was to characterize the spray characteristics and quantify the effect of injection pressure on spray-induced turbulence and air entrainment.

4.1.1 Nozzle Design

Nozzle design is very important when investigating gasoline spray at ultra-high injection pressures. In most of the previous studies of gasoline fuel, a conventional diesel injector was used without any modification. The use of a diesel injector for gasoline fuel is not meaningful since diesel injectors are designed with relatively large L/D ratios (around 8-9) to withstand high pressures. This is in contrast to gasoline

injectors, which are designed with low L/D ratios (around 2-3) to promote better atomization.

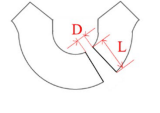
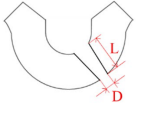
Injector	Injector-1	Injector-2
Hole shape	Divergent	Convergent
Nozzle shape		
Orifice diameter	380 μm	148 μm
L/D ratio	5.45	5.56
Nozzle cone angle	15°	2°
Number of holes	6 holes	
Flow rate	15 mg/ms at 200 bar	

Table 4.1: Specifications of the injector nozzles used in the study.

In this work, prototype injectors were used with L/D ratios higher than typical gasoline injectors to withstand high pressures. However, these ratios were much lower than those for typical diesel injectors. Two axisymmetric nozzle configurations were investigated: divergent and convergent, with orifice hole diameters of 380 μm and 148 μm , respectively. Despite their different geometries and orifice diameters, both nozzles were designed for the same mass flow rate (15 mg/ms at 200 bar). Details of the internal nozzle flow were not simulated because of the unavailability of measured boundary conditions. However, the effect of different nozzle geometries was accounted for by using different spray-jet angles and different coefficients of discharge. Details of the nozzle geometries are summarized in Table 4.1.

4.1.2 Boundary Condition and Numerical Setup

The boundary conditions were the same as in the experiment performed at Chalmers [61]. The boundary conditions are summarized in Table 4.2.

All numerical simulations were carried out using OpenFOAM-2.2.x [62]. The convective scalar fluxes of momentum and time integration were executed using with second-order accurate central differencing scheme and backward scheme, respectively. The spray chamber's boundaries were treated as wall except the bottom of the chamber. All scalar quantities at walls were treated as having a zero-gradient boundary. The spray chamber was maintained at atmospheric conditions ($T=293$ K, $p=1$ bar)

Parameters	Units	Values
Fuel type		n-heptane
Fuel injection pressure	bar	200, 600, 1000, 1500
Fuel injection duration	ms	3.4, 2, 1.5, 1.25
Fuel temperature	K	293
Injection mass	mg	54
Ambient gas		Air
Ambient pressure	bar	1
Ambient temperature	K	293

Table 4.2: Boundary conditions considered in the simulations.

with no initial turbulence. The fuel (n-heptane) was injected using an experimentally determined mass flow rate profile, shown in the Appendix, in the form of spray parcels. The spray-jet angle (extracted from experimental spray images) significantly differed for both nozzle types. The divergent nozzle gave a constant spray-jet angle except during an initial transient period whereas the convergent nozzle gave a varying spray-jet angle. Therefore, the spray-jet angles were set to be a constant 10° and variable from 24° to 5° for the divergent and the convergent nozzles, respectively. The spray submodels used in the simulations are summarised in Table 4.3.

Submodels	Name
Breakup	Reitz-KHRT
Heat Transfer	Ranz-Marshall
Drag	Standard drag model
Collision	none
Atomization	none
Type of spray	Solid cone
Type of injector	Multi-hole injector
Dispersion model	Stochastic dispersion

Table 4.3: The spray submodels used in the spray chamber simulations.

4.1.3 Result Highlights

Liquid Penetration Length

Fig. 4.1 shows the comparison between measured and calculated liquid penetration length for the divergent and the convergent nozzles as a function of time after start of injection (aSOI) at selected injection pressures. The liquid penetration length is defined as a distance of farthest droplet of the spray along the vertical axis of

the spray chamber. The measured data point corresponds to an average of 20 injection shots; the shaded band shows the standard deviation of the experimental data.

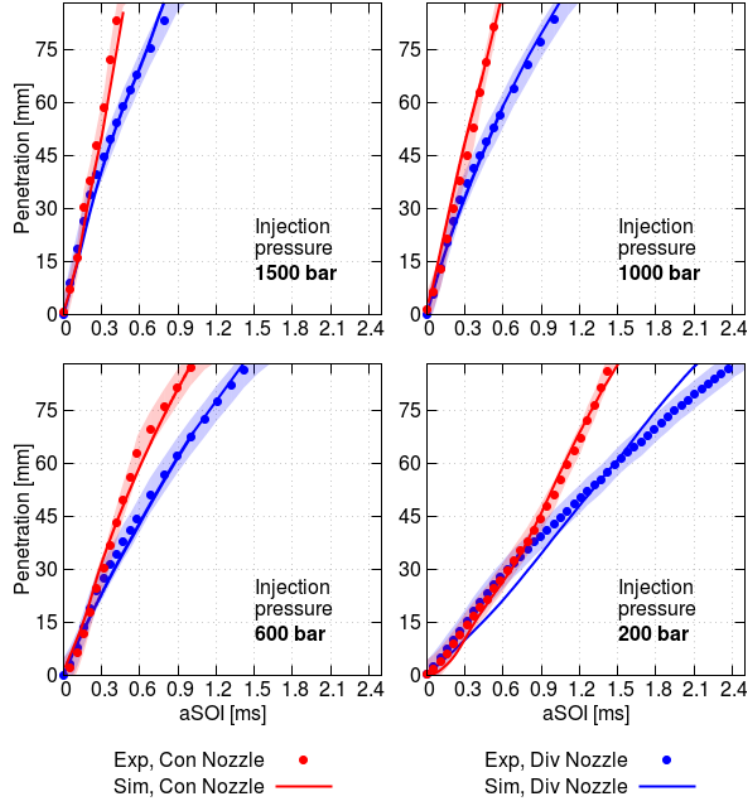


Figure 4.1: Experimental data (point data) and simulation results (line data) of spray liquid penetration length for the divergent and the convergent nozzles at 200, 600, 1000 and 1500 bar injection pressures.

The calculated spray penetration length for both nozzles shows overall good agreement with the experiments. When fuel is injected into the spray chamber, a gas-phase recirculation zone and turbulence are created through momentum transfer from the liquid jet to the gas-phase. In the simulation results, the correct exchange of momentum between the liquid and gas phases, and the correct aerodynamic forces acting on the droplets that strongly influence the atomization process, were ensured by fine-tuning the penetration length to match experimental data. However, some deviation in penetration length was also observed at lower injection pressures. One of the possible reasons behind such a deviation at low injection pressures could be the inaccurate values of the arithmetic mean diameter shown in Fig. 4.2. In general, at all injection pressures, the convergent nozzle has a faster penetration rate, suggesting a faster disintegration of the spray through secondary breakup than with the divergent nozzle.

Overall, the spray-tip penetration suggest that an increase in pressure increases the penetration length and reduces the injection duration significantly. A short injection duration offers more opportunities to adjust the injection timings, for instance, to operate in stratified operation mode or for multiple injection strategies. Also, in the case of early injection, a high injection pressure helps by creating more turbulence to create a homogeneous fuel-air mixture. However, the increasing liquid penetration might also lead to issues of wall wetting at very high injection pressures, and therefore fuel injection timing needs to be properly specified.

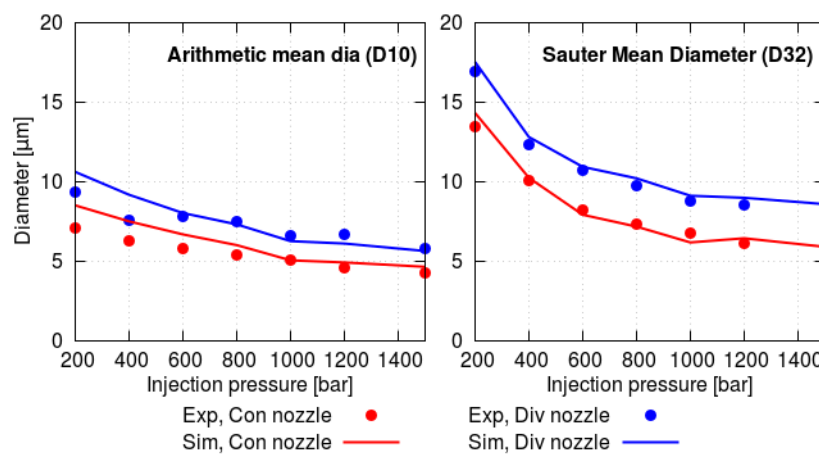


Figure 4.2: Comparison between measured and calculated mean diameter of droplets for the divergent and the convergent nozzle at indicated injection pressures. Right: Arithmetic mean diameter (D10), left: Sauter mean diameter (D32).

Mean Droplet Sizes

Fig. 4.2 shows the comparison between measured and calculated droplet sizes in terms of the arithmetic mean droplet diameter (D10) and the Sauter mean diameter (SMD or D32) at selected injection pressures. The results show the effect of injection pressure on the droplet sizes. In general, the numerical model accurately captures the mean diameter for both nozzles at all injection pressures except for the lower ones. A possible reason for such discrepancy is the considerable high contribution of normal (RT) instability at lower injection pressures compared to those at high injection pressures which are more associated to higher shear (KH) instability. The results confirm the well-known result that droplet sizes decrease with increasing injection pressure, irrespective of nozzle shape. Moreover, the mean droplet diameters (D10 and D32) for the divergent nozzle exceed those for the convergent nozzle, irrespective

of injection pressure. However, the arithmetic mean droplet diameter (D_{10}) varies less than the SMD. At high injection pressures, droplets quickly reach their stable diameter below which no secondary breakup occurs. A small diameter value (or small droplet size) means a large contact surface area of the droplet, which is beneficial for faster evaporation under real engine conditions.

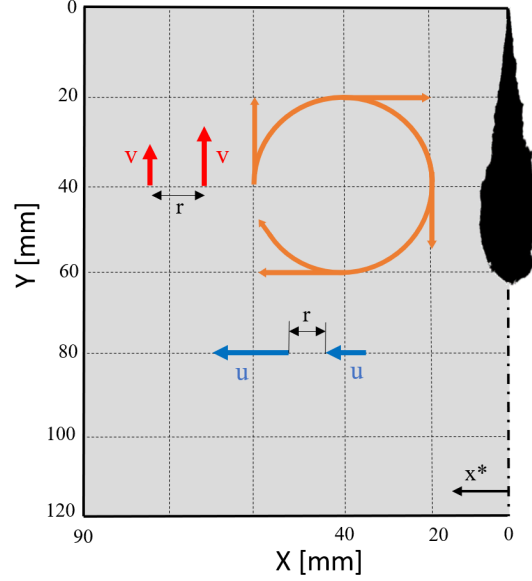


Figure 4.3: A sample position of a spray-generated big vortex. The velocity vectors u and v shown for the illustration of the definition of the two-point correlation functions.

Spray-Induced Large Scales

One of the potential benefits of ultra-high fuel injection pressures is the enhancement of spray-induced turbulence which can be used to promote efficient fuel-air mixing. As the fuel is injected at high velocities into the spray chamber, the ambient gas quickly becomes turbulent due to strong momentum exchange between the liquid spray and the gas phase. The largest scale of turbulence i.e. integral length scale can be calculated using the velocity correlation, as:

$$L_\delta = \int_0^q \frac{u'_\alpha(z) u'_\alpha(z+r)}{u'_\alpha(z)^2} dr. \quad (4.1)$$

Here, u'_α is the velocity fluctuation in the α direction, r is the distance between the two velocity vectors, and q is the length of the probe line. This classical two-point correlation is realistic for homogeneous, isotropic turbulence with sufficient

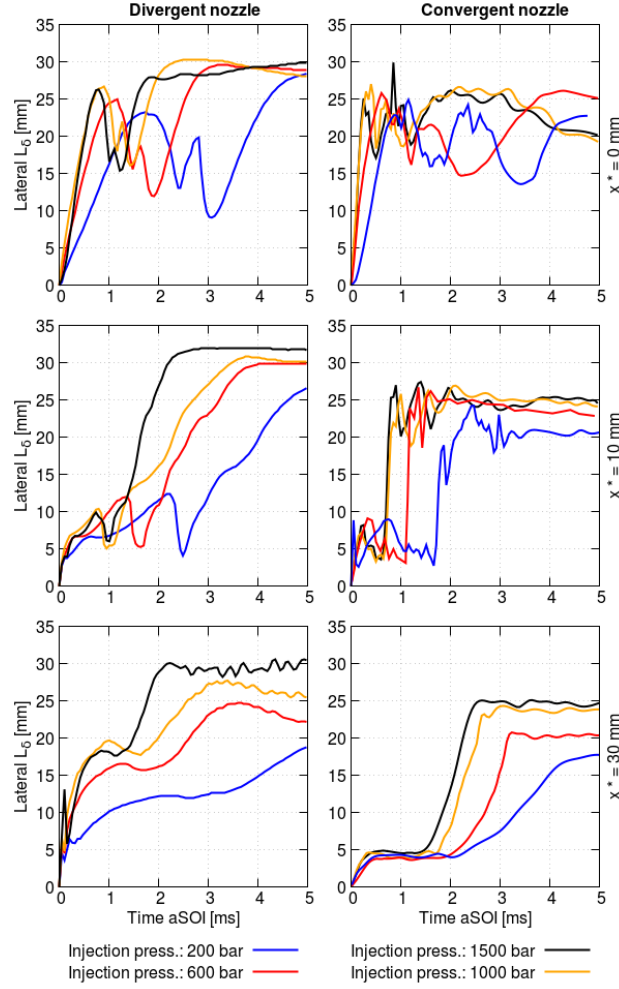


Figure 4.4: Integral length scale as a function of time calculated on the spray axis (top left and right), and on a vertical line at radial locations of 10 mm and 30 mm parallel to the spray-axis (middle and bottom left and right) for the divergent and the convergent nozzles at 200, 600, 1000 and 1500 bar injection pressures.

statistical data which are often not available when investigating highly transient sprays. Therefore, we used an alternative definition [63] that includes vortex and subsequent coherent structures:

$$L_\delta = \int_0^q \frac{u_\alpha^\delta(z) u_\alpha^\delta(z+r)}{u_\alpha^\delta(z)^2} dr, \quad (4.2)$$

here u^δ is the deviation of the instantaneous (filtered) velocity \tilde{u} from the spatial mean value $\bar{\tilde{u}}$ along a probe line. The modified function to calculate the integral length scale (Eqn. 4.2) is evaluated at 3 different vertical locations: $x^*=0$ mm, $x^*=10$ mm and $x^*=30$ mm (illustrated in Fig. 4.3). Fig. 4.4 shows the integral length scale at selected injection pressures for both nozzles at three probe locations. As a

general trend, it can be observed that higher fuel injection pressures tend to generate larger turbulence structures more quickly than lower injection pressures. This is particularly obvious for the divergent nozzle. The final scale of the integral length scale does not depend much on the fuel injection pressure for a given nozzle type particularly along the spray axis ($x^*=0$ mm). However, the integral length scales at radial locations ($x^*=10$ mm and $x^*=30$ mm) clearly show the effect of higher injection pressures such as substantially larger length scales at the highest pressure compared to the lowest. Similar trends can be observed for the convergent nozzle with steeper gradients during the creation of large turbulent eddies by the spray. The spray from the divergent nozzle creates slightly larger turbulence length scales which may have the potential to survive longer.

Air Entrainment

Efficient fuel-air mixing in a direct fuel injection system strongly depends on the air entrainment rate. Here, the air entrainment is quantified as the mass fluxes across a control line of length 40 mm (see Fig. 4.5) at selected injection pressures. All the velocity vectors on the probe line pointing towards and perpendicular to the spray-axis were considered to be air entrainment.

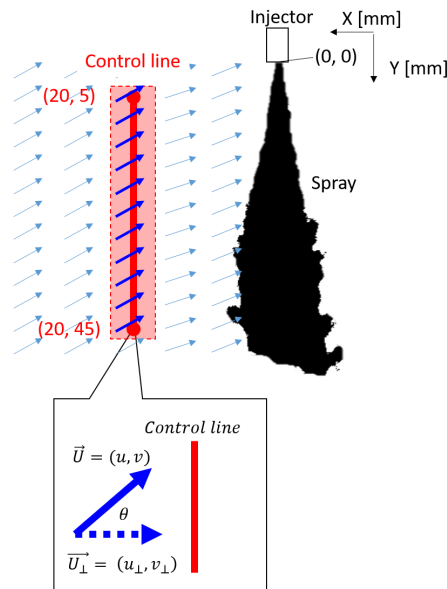


Figure 4.5: The control line for air entrainment rate calculation.

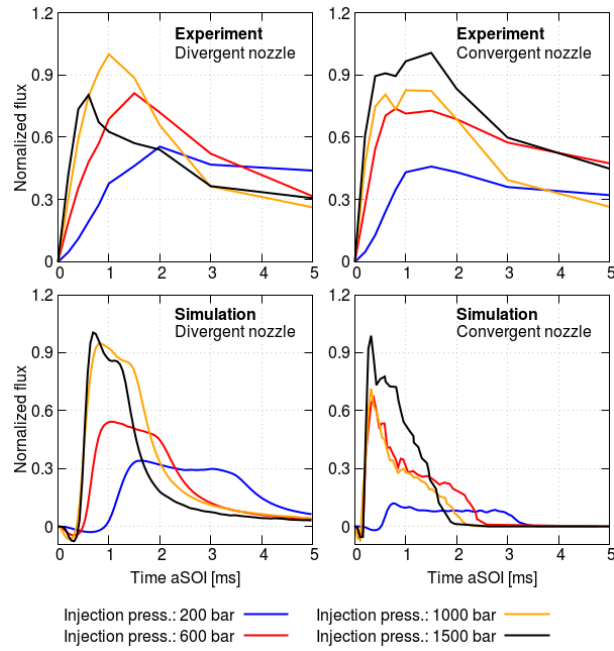


Figure 4.6: Total air entrained over the control line for the divergent and convergent nozzles at 200, 600, 1000 and 1500 bar injection pressures.

The development of the normalized air entrainment rate during the complete injection process is summarized in Fig. 4.6. The results indicate that the entrainment rate is significantly affected by the injection pressure, that is, the entrainment rate is increased by injecting the fuel at higher pressures. A similar result can be seen for both nozzle types. However, entrainment for the convergent nozzle dies out quickly while it persists longer for the divergent nozzle at the respective pressures. This result suggests that the divergent nozzle is more effective at maintaining the flow motion.

4.2 Optical GDI Engine

For this test, fuel was injected inside the optical GDI engine at selected injection pressures. Based on the overall conclusion from the previous part on the nozzle shape, only the divergent shaped nozzle was used, as it performed the best. For details of the experimental configuration of the optical GDI engine, please refer to Paper 1. The main aim of this part of the study was to quantify the fuel-air mixture homogeneity, spray-induced turbulence and fuel mass deposition, as well as the evolution of fuel film.

4.2.1 Mesh Handling and Mesh Motion

In this work, the entire meshing work was carried out using a fully automated tool based on OpenFOAM's mesh generation utilities. The blockMesh and snapPyHexMesh tools were used to create a block around the entire geometry, and for geometry-based sculpting of the mesh, respectively. The valves were closed by internal walls called "curtains" around the valve seat regions. Fig. 4.7 shows the complete computational domain, cylinder head with the grids, and the grids on the cutting plane through the geometric center of the cylinder. The grids mostly consisted of equidistant hexahedral cells with a local mesh refinement around the spark plug, injector and valve seat regions. The average grid cell sizes inside the combustion chamber, near the spark plug and around the valve seat region were 0.5, 0.2 and 0.1-0.4 mm, respectively. The mesh resolution at the intake and exhaust port was reduced to 1.5 mm.

Mesh motion was combined with a mapping strategy where each mesh was only valid for a certain crank angle interval. The calculated result at the end of each interval was mapped onto a new pre-generated mesh for every 5 CAD. The simulation then continued for the new-interval. In total, 144 grids were used for a full-cycle simulation. This procedure ensured a high mesh quality over the whole numerical simulation. The mapping approach is shown in Fig. 4.8. For the mesh motion, a Laplacian Equation (Eqn. 4.3) describing the cell displacement x_c was solved [64, 65]:

$$\frac{\partial}{\partial x_k} \left(\gamma \frac{\partial x_{c,k}}{\partial x_k} \right) = 0. \quad (4.3)$$

A smooth mesh deformation was controlled by introducing an artificial stiffness γ , which can be expressed as a function of the distance between the moving boundaries. Here, the stiffness was calculated as the quadratic inverse distance l^2 to the cylinder

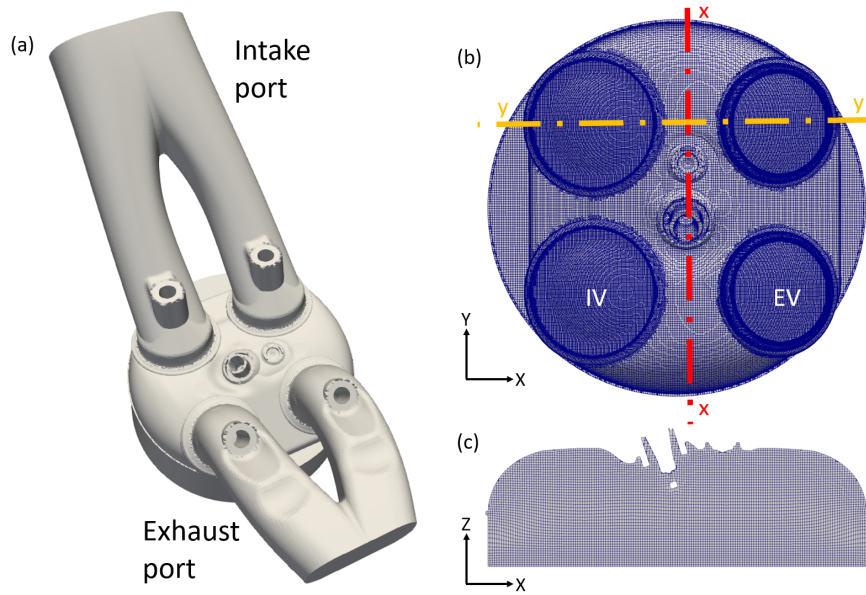


Figure 4.7: (a) Complete computational domain, (b) top view of the cylinder head grid, (c) grids in the xx -plane.

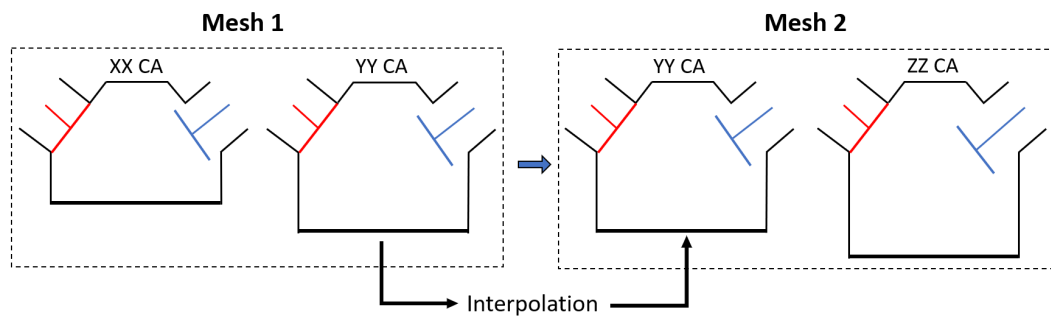


Figure 4.8: Illustration of the mapping approach used to cover full-cycle simulation.

head and piston:

$$\gamma = \frac{1}{l^2}. \quad (4.4)$$

After solving the mesh motion equation, the displacement of the cell nodes was calculated with respect to reference position ($x_{\text{ref},k}$), as:

$$x_k^{\text{new}} = x_{\text{ref},k} + x_{\text{disp},k}. \quad (4.5)$$

4.2.2 Boundary Condition and Numerical Setup

In total, four consecutive cold flow LES full-cycles were simulated to generate realistic in-cylinder turbulence. The initial three cycles were ignored due to dilution from the initial boundary conditions, so the last cycle was used to carry out the spray injection simulations at each selected injection pressure. Specifications of the optical engine and the boundary conditions are summarized in Table 4.4. And, the numerical submodels used are mentioned in the Table 4.5.

Parameters	Units	Values
Bore/Stroke	mm	86/92
Compression ratio		10
Engine speed	rpm	1750
Intake Valve Open/Close	CAD	0/235
Exhaust Valve Open/Close	CAD	480/720
Fuel		iso-Octane
Fuel injection pressure	bar	200, 600, 1000, 1500
Nozzle cone angle	°	15
Nozzle orifice diameter	μm	380
Cylinder head temperature	K	361
Liner temperature	K	353
Piston temperature	K	368
Intake air temperature	K	298

Table 4.4: Specifications and boundary conditions of the optical research engine.

Submodels	Name
Breakup	Reitz-KHRT
Heat Transfer	Ranz-Marshall
Drag	Standard drag model
Collision	none
Atomization	none
Type of spray	Solid cone
Type of injector	Multi-hole injector
Dispersion model	Stochastic dispersion
Wall model	Bai-Gosman

Table 4.5: The spray submodels used in the engine simulations.

A time-dependent measured absolute pressure profile was imposed at the inlet and outlet. A zero-gradient boundary condition was applied for all scalar quantities at walls, with a no-slip boundary condition for velocity (except for the piston and

valves). The piston and liner surfaces were discretized using the finite area method to solve the equations governing the fuel's liquid-film evolution. The time integration was carried out using an implicit second-order accurate backward differencing scheme. Convective fluxes of the momentum were modeled using a pure second-order accurate central differencing scheme. The time-step width was calculated using the convective Courant-Friedrichs-Lewy (CFL) criterion with a maximum CFL number of 0.5.

In the spray simulations, liquid fuel (iso-Octane) was injected into the engine at selected injection pressures. Before starting the spray injection, the gas-phase (air) inside the engine was already turbulent (developed by running consecutive LES cycles). Monodispersed droplets (blobs) with an initial diameter, as calculated by Eqn. 3.47, were injected based on the experimentally determined mass flow rate profile (shown in the Appendix). The spray-jet angle extracted from experimental spray images was used as an input value. Primary breakup and secondary breakup were modeled using the blob injection model and KH-RT model, respectively. A stochastic dispersion model was used to account for the turbulent fluctuations in droplet trajectories. The spray impingement on the engine walls was modeled with a detailed liquid wall-film model tracking the evolution of the area and thickness of the liquid-film. This was achieved by solving equations for the liquid mass (Eqn. 3.73), momentum (Eqn. 3.76) and energy (Eqn. 3.77) using the Finite-Area discretization method.

4.2.3 Result Highlights

LES Quality Criterion

The quality of LES simulations can be evaluated by the fraction of the turbulent kinetic energy resolved on the grid as suggested by Pope [66]. That fraction can be evaluated by the ratio of the turbulent kinetic energy calculated by the sub-grid scale model to the total turbulent kinetic energy in each cell:

$$M(\mathbf{x}, t) = \frac{K_{sg}(\mathbf{x}, t)}{K_r(\mathbf{x}, t) + K_{sg}(\mathbf{x}, t)}. \quad (4.6)$$

Here, $K_{sg}(\mathbf{x}, t)$ is the sub-grid scale turbulent kinetic energy (which is modeled) and $K_r(\mathbf{x}, t)$ denotes the resolved turbulent kinetic energy at a specific location \mathbf{x} and time t . The value of $M(\mathbf{x}, t)$ varies between 0 and 1: $M = 0$ corresponds to a fully resolved turbulent velocity field (DNS) and $M = 1$ means that all turbulent fluctuations are modeled (RANS). A value of $M(\mathbf{x}, t)$ for a good quality LES simulation

should not exceed 0.2, which means that 80% of the turbulent kinetic energy should be resolved.

Fig. 4.9 shows the domain averaged value of M during the entire cycle of cold flow

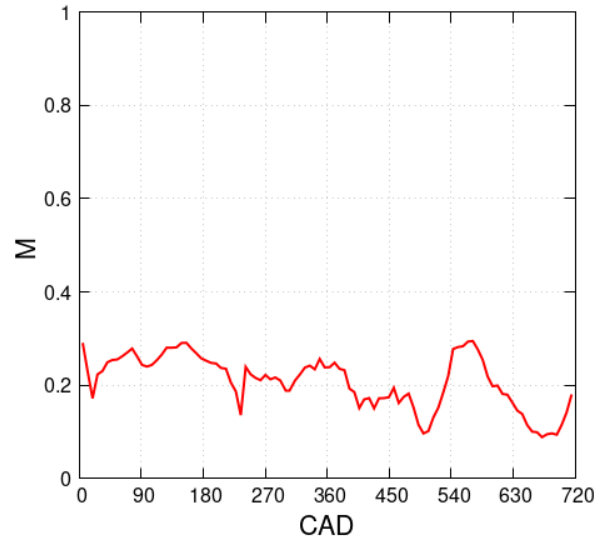


Figure 4.9: The average value of M during the entire cycle.

simulation. The plot shows that the criterion (for a good LES) is satisfied for most parts of the entire cycle. Some undesired high peaks are also visible especially during intake and exhaust strokes.

In-cylinder Cold Flow

Before the spray simulations, cold flow full-cycle simulations were carried out to generate realistic in-cylinder turbulence. In total, four cycles were run, with the first three cycles being ignored to minimize the impact of initial boundary conditions. The turbulence generated in the last cycle was used as the initial condition for the spray simulations. The validity of the methodology and setup used in terms of mesh and boundary conditions was verified by comparing calculated and experimental profiles of in-cylinder pressure traces, as shown in Fig. 4.10. Good agreement was obtained, a fundamental requirement for successful simulation of fuel-air mixing processes [67].

Fig. 4.11 shows snapshots of the in-cylinder flow motion at selected instances (including the SOI timings considered here), showing the flow field's evolution during the last cycle on the valve center plane (yy -plane, Fig. 4.7). The incoming air flow is

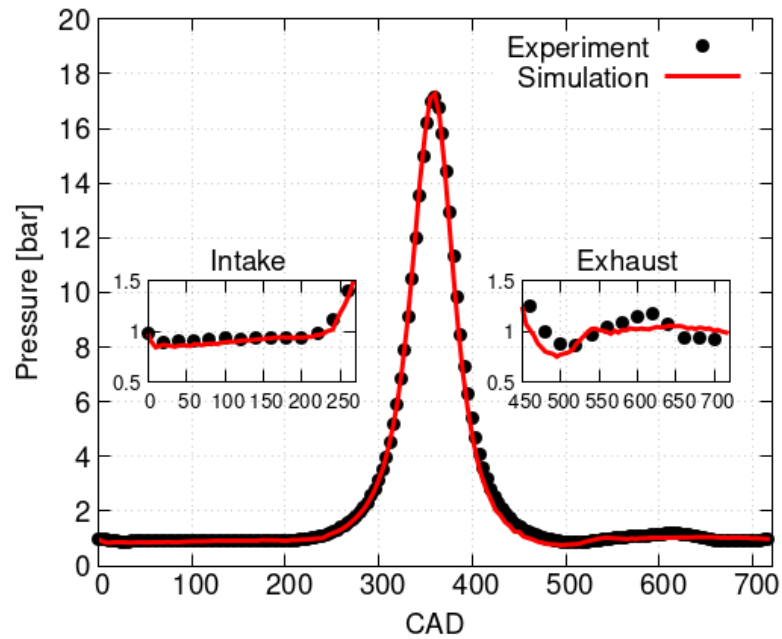


Figure 4.10: The comparison of in-cylinder pressure traces for a cold flow full cycle with the experimental data.

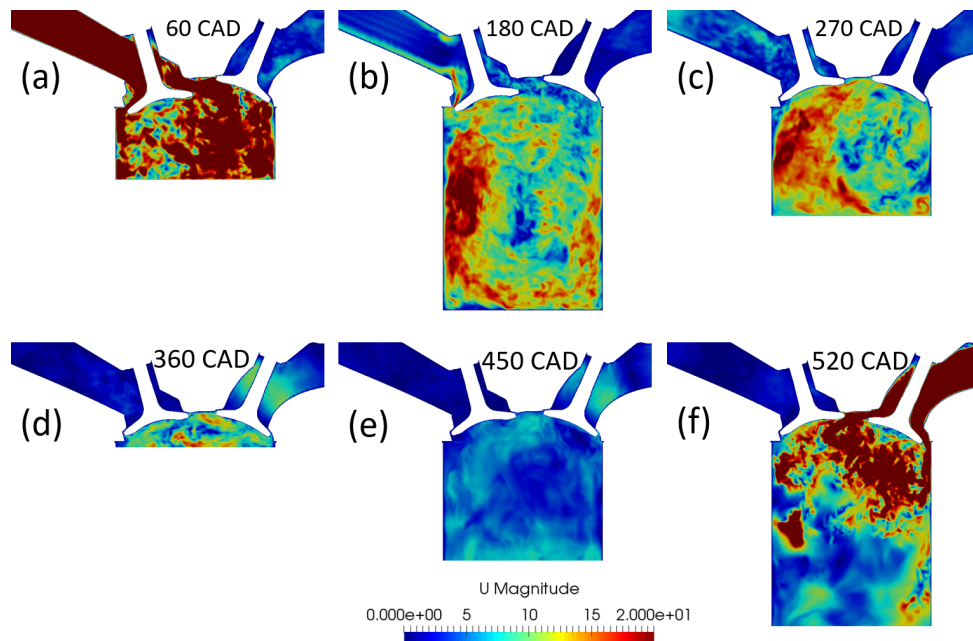


Figure 4.11: Evolution of the in-cylinder flow field, showing simulated fields: (a) during intake, (b) at bottom dead center, (c) during compression, (d) at top dead center, (e) during expansion, and (f) during exhaust.

described in terms of velocity across this plane. Propagation of a counter-rotating vortex on the bottom of the intake valve can be seen. The intake port was designed to generate tumble mostly from the upper side of the valve, as can be seen in Fig. 4.11a. The intake valve was closed at 235 CAD and the flow field generated during compression is shown in Fig. 4.11c. The tumble generated during the intake stroke was well preserved during the compression phase. Opening of the exhaust valve (at 480 CAD) initiated an enormous flow flux in the cylinder, due to the pressure difference, and continued as fluids were expelled when the piston moved upward. Unfortunately, no experimental data are available to verify the in-cylinder turbulence observed in the simulations.

Spray evolution

Figure 4.12 shows a comparison of computed spray evolution and high-speed camera images at selected injection pressures. The captured images comprise an average of 20 shots. In simulations, all six spray jets were taken into account for appropriate comparison with experimental images. The results show that the overall spray shape was well predicted by the numerical models.

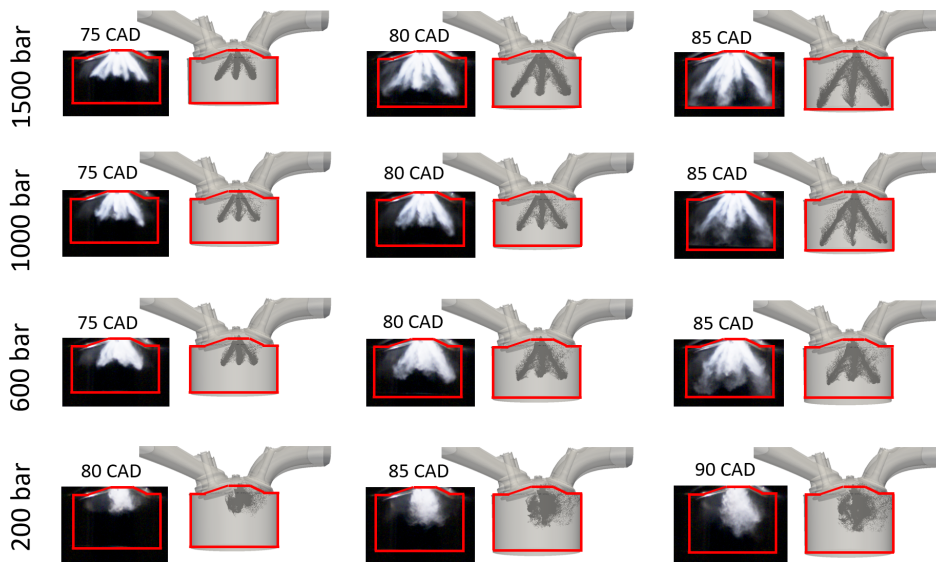


Figure 4.12: Comparison of measured and calculated spray images at the indicated CAD and injection pressures.

These images show the highly transient behavior of the spray when it penetrates into the cylinder. At low injection pressures, the fuel jets interact heavily with the tumble motion, resulting in a fuel cloud with no visible individual fuel jets. In contrast, at a high injection pressure, the spray has very high velocity and momentum, so

the tumble motion generated during the intake stroke has much less effect on it. The numerical simulations accurately captured the overall spray shapes, showing detached spray jets at high injection pressures and amalgamated jets at low injection pressures.

Spray-Induced Turbulence

Once the simulations of the engine cycle provided a realistic flow field, fuel was injected at selected injection pressures to investigate the fuel-air mixture formation. The in-cylinder turbulence is mostly generated by large-scale gas motion, which quickly breaks down into small-scale vortical motion. In-cylinder turbulence is a very important feature to investigate as it strongly influences the fuel-air formation. A potential benefit of injecting fuel at ultra-high pressures is enhancement of the overall turbulence level through strong momentum exchange between the spray and the gas.

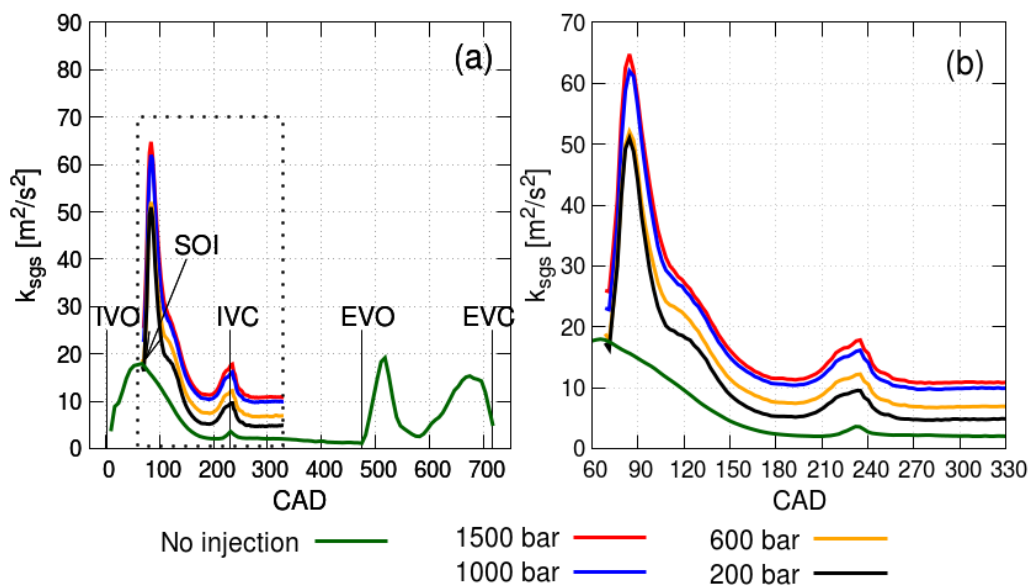


Figure 4.13: (a) Evolution of turbulent kinetic energy during a complete flow cycle and with injection at indicated pressures, (b) magnified view of area within dotted lines in (a).

To quantify the in-cylinder turbulence, the evolution of the total turbulent kinetic energy (TKE) inside the cylinder during a complete cycle and after fuel injection at each injection pressure was compared, as shown in Fig. 4.13. Without injection, very strong turbulence is generated during valve opening and closing, but TKE levels stay minimal after intake valve close (IVC) and during the compression stroke. Fig.

4.13b shows a magnified view of the dotted area marked in Fig. 4.13a, and clearly indicates the increases in turbulence levels associated with increases in injection pressure. Even if the TKE levels quickly decrease after fuel injection, higher TKE levels induced by the spray remain present until the spray ignition point (at 330 CAD). Overall, results indicate that the fuel injection boosts the turbulence level, in an injection pressure-dependent manner, indicating that momentum transfer from the liquid to gas phase significantly increases the total TKE in the cylinder. An additional interesting observation for the injector used here is that TKE does not increase much further with increases in injection pressure beyond 1000 bar.

Fuel-Air Mixture Homogeneity

To understand the influence of injection pressure on the fuel-air mixing process, the evolution of the overall mixture homogeneity was investigated. The fuel-air mixture homogeneity was assessed using the uniformity index [68], defined as:

$$U.I. = 1 - \frac{\sqrt{\sum_{i=1}^N (\bar{F} - F_i)^2}}{\sqrt{A/F/(1 + A/F)}}, \quad (4.7)$$

$$\text{with, } \bar{F} = \frac{\sum_{i=1}^N F_i V_i}{\sum_{i=1}^N V_i}.$$

Here, F and A/F represent the fuel mass and air-fuel mass ratio of perfectly mixed mixture, respectively and V denotes the mesh cell volume with total number of cells N .

Fig. 4.14 shows the evolution of the uniformity index from the SOI (60 CAD) to spark ignition point (330 CAD). It clearly shows that increasing the injection pressure enhances the fuel-air mixture homogeneity. Note that the uniformity index used here expresses a domain-average quantity and thus does not provide any information about the presence of locally fuel-rich areas.

Fuel Mass Budget and Film Thickness

Fig. 4.15 shows CAD-resolved total liquid masses (droplets plus wall-film), liquid masses deposited on the walls (fuel films), and fuel vapor masses at the selected injection pressures. It clearly shows that increasing the injection pressure leads to faster injection of the fuel (i.e. shorter injection durations, as shown in Fig. 7.1 in the Appendix), faster overall evaporation (from droplets and film) and quicker

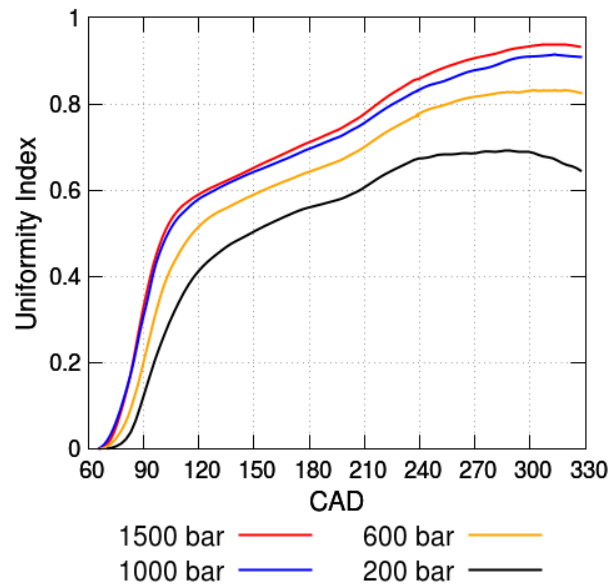


Figure 4.14: The progression of the uniformity index at indicated injection pressures with respect to CAD.

build-up and evaporation of the liquid-film. At low injection pressures, the fuel injection duration is longer and larger droplets form (cf. Fig. 4.2) leading to slower evaporation. Moreover, Fig. 4.15b shows that increasing the fuel injection pressures leads not only to less accumulation of liquid mass on the walls, but also to faster evaporation after the maximum film mass has been reached.

As a result of the faster disintegration and evaporation of fuel droplets at high injection pressures, fuel droplets evaporate more quicker and less fuel is deposited on the walls than at lower pressures. On the other hand, lower injection pressures lead to deposition of quite large amounts of fuel onto the walls, which could significantly contribute to the particulate emissions, as shown in Fig. 7.3. This correlation can only be speculative here as the optical engine tests were carried out in cold conditions (without firing the engine), however, the observed trends regarding the reduction of liquid-film mass with increasing injection pressure should be similar.

Fig. 4.16 shows the evolution of the liquid-film area and film thickness at the selected injection pressures. The results clearly show that injecting fuel at higher pressures advantageously increases the liquid-film area with consequent reductions in film thickness. The fuel film area continuously shrinks after the peak due to evaporation. However, the film thickness increases close to top dead center (TDC) because the fuel deposited on the walls begins to concentrate in a very small region

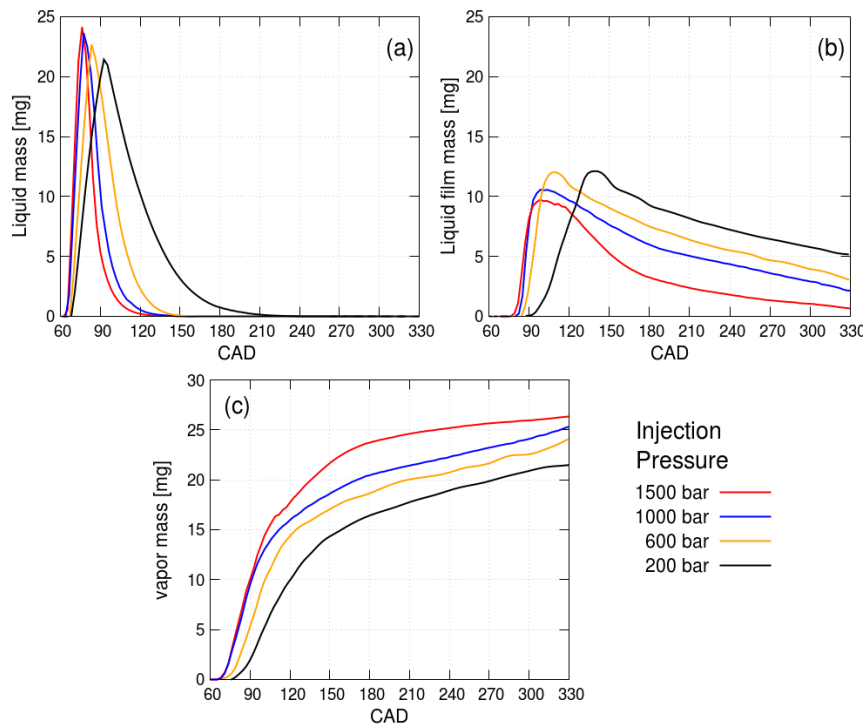


Figure 4.15: The fuel mass budget: (a) liquid masses, (b) liquid-film masses, and (c) vapor masses at indicated injection pressures with respect to CAD.

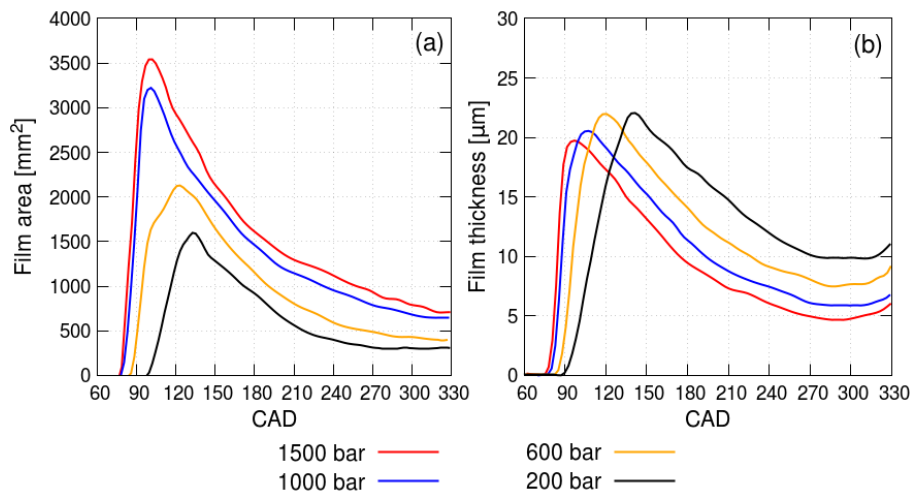


Figure 4.16: The evolution of liquid-film area (left) and film thickness (right) at indicated injection pressures with respect to CAD.

and consequently the evaporation rate is very low. The concentration of fuel in a small area leads to pronounced local fuel-rich zones, which are primary contributors of particulate emissions.

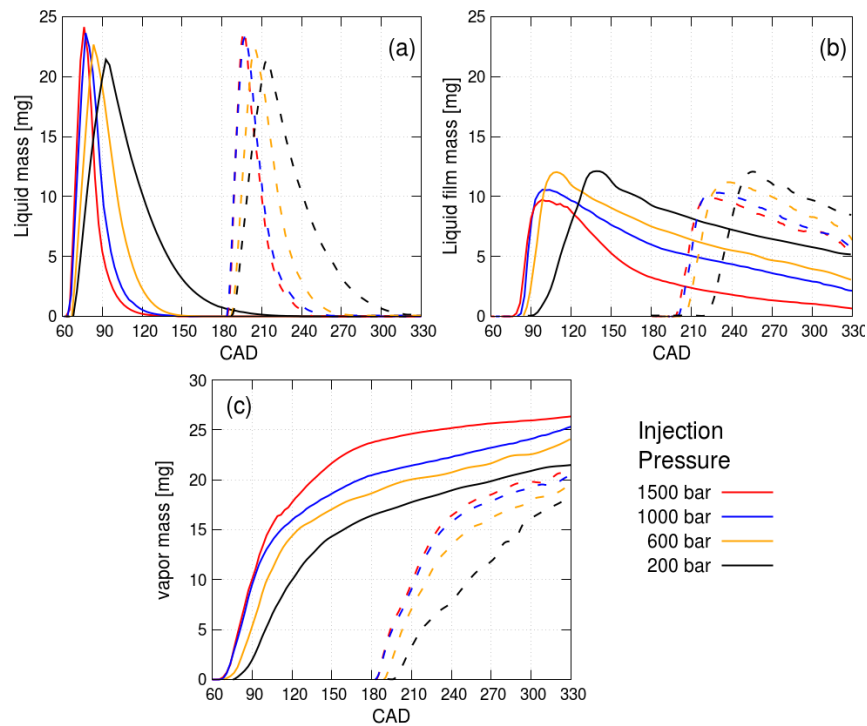


Figure 4.17: Liquid fuel mass budgets: (a) liquid masses, (b) liquid film masses, and (c) vapor masses at indicated injection pressures with early injection (60 CAD) and late injection (180 CAD).

Fig. 4.17 shows the CAD-resolved fuel film thickness at the selected injection pressures for both early and late injection timings. With early injection, the fuel film is thinner than with a corresponding late injection. With early injection, fuel film formed has adequate time to evaporate and the resultant fuel film becomes thinner. In contrast, in late injection, fuel is injected after BDC when the piston is moving upwards, which causes the liquid film to be pushed upwards by the piston rings and thus become thicker.

Chapter 5

Conclusion and Outlook

The presented study investigated the potential benefits and limitations of ultra-high pressure fuel injection technique in GDI engine application. Large-Eddy Simulations were carried out to investigate the development of gasoline spray at ultra-high injection pressures (200-1500 bar) in a constant volume spray chamber and in an optical GDI engine to answer the research questions stated in Chapter 1. The main findings obtained are summarized below.

- The numerical model was able to reproduce the experimentally observed liquid penetration length after fine-tuning of an arbitrarily chosen case (i.e. 1000 bar case). However, some deviations in liquid penetration length were observed at lower injection pressures. At higher injection pressures, the injection duration was significantly reduced and offering more flexibility for advanced injection strategies. The spray at higher injection pressures had very higher momentum, thereby increasing the risk of hitting the engine wall.
- Simulated mean droplet diameters (D10 and D32) agreed well with experimental data. The results revealed that the atomization was very sensitive to the injection pressure. Droplet sizes were significantly reduced by increasing the injection pressure from 200 to 800 bar, but increasing the injection pressure even higher showed only a marginal impact on droplet sizes. At lower injection pressures, the mean droplet diameter agreed less with the measured values, possibly because of high contribution of normal (RT) instability than shear (KH) instability. Fuel droplets from the liquid fuel jet are disintegrated into smaller droplets more rapidly, which is beneficial for quick evaporation, thereby promotes better mixing at higher injection pressures.

- The divergent nozzle shows overhead compared to convergent type nozzle. The droplet mean values are lower for convergent nozzle but extremely high penetration length and overall narrow spray structure asides such benefit. Moreover, the divergent nozzle shows higher air entrainment at the same injection pressures which suggests that the divergent nozzle helps to create and maintain spray-induced vertexes. The air entrainment for the convergent nozzle spray at high injection pressures is high at the beginning but dies-out quicker compared to the divergent nozzle at the same injection pressures.
- At higher fuel injection pressures, the fuel spray carries higher momentum into the cylinder, so there is higher turbulent kinetic energy. This contribution is known as spray-induced turbulence. Estimated integral length scales of the spray-induced turbulence turned out to be larger at high injection pressures compared to lower ones. At low injection pressures, in-cylinder turbulence has a more dominant effect than the spray velocity, thereby the spray jet struggles to penetrate the tumble, resulting in amalgamated spray structure.
- Increases in injection pressure increase overall homogeneity of the fuel-air mixture, as indicated by the uniformity index. The differences between the uniformity index at the lowest injection pressure (200 bar) and the highest injection pressure (1500 bar) were considerably large, but the differences in uniformity index between the higher injection pressures were relatively low.
- The evolution of fuel masses (droplets, film, vapor) indicates that fuel evaporates more quickly at higher injection pressures due to the formation of smaller fuel droplets and a thinner liquid wall-film. However, at low injection pressures, the injection duration is longer and higher masses of fuel are deposited on the walls. The resulting local fuel-rich zones are likely the main reason for high PN emission.
- One of the benefits of higher pressure fuel injection is that they increases the liquid-film area on the surface, so the film is thinner, leading to faster evaporation of the liquid-film.
- The results demonstrate that injection pressures of 1500 and 1000 bar provide similar overall performance. The upper threshold, above which any further improvements (if any) are marginal, is likely injector-dependent, but it might be a general rule that each injector has such a threshold, related to pressure surging and choking effects inside the injector. It is therefore not useful to increase the injection pressure above these injector-dependent values.

Chapter 6

Future Work

Despite answering some of the important research questions related to the potential for enhancing the fuel injection pressure in GDI engines, this research has also left some unanswered questions that could be addressed in future investigations.

- It would be interesting to see an investigation of in-nozzle flow through different nozzle shapes and, in particular, how the cavitation affects flow and liquid ligaments as they emerge from the nozzle.
- It would be interesting to see a wall-film development under realistic engine conditions such high temperature, high load and at higher engine speed conditions.
- It would be interesting to see the results from combustion and soot modeling for the fuel-air mixture prepared at ultra-high injection pressures.
- It would be interesting to see the integration of advance concept such as multiple injection into the high injection pressure technique.

Chapter 7

Summary of Publications

Paper 1

“Large-Eddy Simulation of Spray-Turbulence-Wall interaction in a Gasoline Direct Injection Engine at Ultra-high Injection Pressures”

Authors: **S. Wadekar** and M. Oevermann

Submitted to "International Journal of Multiphase Flow", 2021

In this work, numerical simulations using the Large-Eddy Simulation (LES) method were carried out to investigate fuel-air mixture formation inside a gasoline direct injection engine at ultra-high injection pressures. In our models, the Large-Eddy Simulation (LES) method for simulating turbulent flows was utilized in combination with a Lagrangian approach to model the fuel spray. Interaction of the liquid spray with the piston and cylinder walls was taken into account by using a finite-area wall-film module, which allowed tracking of the liquid fuel mass deposited on the walls and its evaporation from the wall. We validated the simulation approach and spray model with data obtained from experiments using a constant volume spray chamber. Following full-cycle engine simulations, a representative low-load case on the optical engine was performed to generate initial turbulence inside the engine cylinder for subsequent investigations of the fuel-air mixing and spray dynamics under various high and ultra-high fuel injection pressures. The simulation results showed that spray-induced turbulence increases with increasing fuel injection pressure, thereby increasing mixture homogeneity. The liquid fuel mass deposited on the walls, i.e. fuel film, is significantly reduced at high injection pressures owing to the faster fuel disintegration and evaporation.

Division of work: S. Wadekar developed the code, ran all the simulations, wrote the paper and generated all figures and tables. M. Oevermann was responsible for project acquisition and conceptualization, discussions, corrections and proof-reading.

Paper 2

“Large-Eddy Simulation Study of Ultra-High Fuel Injection Pressure on Gasoline Spray”

Authors: **S. Wadekar**, A. Yamaguchi and M. Oevermann

Published in Journal "Flow Turbulence and Combustion", 2020

In this work, numerical simulations were carried out to simulate gasoline injection inside a constant volume chamber at ultra-high injection pressures using the Large-Eddy Simulation (LES) method. Two different nozzle hole geometries, divergent and convergent, were used with injection pressures ranging from 200 to 1500 bar. A well-known Eulerian-Lagrangian (LES-LPT) framework was used along with different sub-models. At first, numerical results were calibrated by reproducing experimentally observed liquid penetration lengths and efforts were made to understand the effect of ultra-high injection pressures on the spray development. The calibrated models were then used to investigate the effect of ultra-high injection pressures on mean droplet sizes, droplet size distribution, spray-induced large-scale eddies and entrainment rate. The results concluded that the ultra-high injection pressures significantly reduced the mean droplet sizes for both nozzle shapes. The integral length scales of spray-induced turbulence and air entrainment rate were better for the divergent injector and considerably larger at higher injection pressures compared to lower ones.

Division of work: S. Wadekar developed the code, ran all the simulations, wrote the paper and generated all figures and tables. A. Yamaguchi provided the experimental data. M. Oevermann was responsible for project acquisition and conceptualization, discussions, corrections and proof-reading.

Paper 3

“Large-eddy simulation on the effects of fuel injection pressure on the gasoline spray characteristics”

Authors: **S. Wadekar**, A. Yamaguchi and M. Oevermann

Published in "SAE International Powertrains Fuels and Lubricants", 2019, San Antonio, USA

In this work, a gasoline fuel spray was investigated for divergent type nozzle over a range of fuel injection pressures from 400 to 1500 bar using numerical simulations. The numerical calculations were carried out for a constant volume chamber under non-vaporizing conditions to best match the experimental setup. Large-eddy simulation (LES) was used for the gas flow and a standard Lagrangian spray model for the liquid phase was utilized. The spray atomization was modeled using the Kelvin Helmholtz - Rayleigh Taylor (KH-RT) atomization model with a droplet size distribution from the injector assumed to follow a Rosin-Rammler distribution function. Simulation results for the spray liquid penetration length were validated with experimental findings under different fuel injection pressures. Afterwards, arithmetic mean droplet diameters (D10) and a Sauter mean droplet diameters (D32) as a function of pressure were compared against the measured droplet diameters. Simulated drop size distributions were compared with measured droplet sizes. The results indicated that a high fuel injection pressure increases the liquid penetration length and significantly reduces droplet sizes. The results also showed good agreement for overall spray structure, time-resolved droplet size, mean droplet sizes (D10 and D32) and droplet size distribution.

Division of work: S. Wadekar developed the code, ran all the simulations, wrote the paper and generated all figures and tables. A. Yamaguchi provided the experimental data. M. Oevermann was responsible for project acquisition and conceptualization, discussions, corrections and proof-reading.

Paper 4 & 5

“Large-eddy simulation study of combustion cyclic variation in a lean-burn spark ignition engine”

Authors: **S. Wadekar**, P. Janas and M. Oevermann

Published in journal "Applied Energy", 2019

In this work, multi-cycle Large-Eddy Simulation (LES) was carried out to investigate combustion cyclic variability (CCV) in a single cylinder spark ignition engine with a homogeneous lean ($\lambda=1.25$) iso-octane-air mixture. The main objective of this study was to obtain physical insights into the early stage of combustion and its influence on CCV. Propagation of the flame was modeled using a transport equation for the filtered flame surface density within the LES framework. An advanced spark-ignition (ISSIM-LES) model was implemented which provided the resolved flame kernel information from the spray discharge. Ten consecutive cold flow LES cycles followed by two initialization cycles (12 cycles in total) were used to run the reactive simulations concurrently. The simulation results were compared with experimental data. Although the number of computed cycles was fairly low, the LES was able to reproduce the cyclic variability observed in experiments both quantitatively and qualitatively. Validation of the simulation was done by comparing the measured pressure traces. Then, correlations between the timing of the 10% fuel burnt mass fraction with early flame kernel growth and initial-to-turbulent transition period (in which there was an asymmetric flame kernel that persisted through the early development periods) were determined. The calculated results of the flame propagation were then analyzed at two cross-sections (in the swirl and tumble planes) of the combustion chamber, which highlighted differences in instantaneous flame structures and propagation characteristics between the fastest and slowest cycles. Good overall agreement was obtained between the measurements and simulation data. The results revealed that the instantaneous velocity and fluctuation of flows around the spark vicinity affect growth of the early flame kernel and cause combustion cyclic variability.

Division of work: S. Wadekar developed and implemented the models in the code, ran all the simulations, wrote the paper and generated all figures and tables. P. Janas provided the cold flow LES cycles and contributed in correction, and M. Oevermann contributed corrections, discussions and proof-reading.

Paper 6

“Large Eddy Simulation of Stratified Combustion in Spray-Guided Direct Injection Spray-ignition engine”

Authors: **S. Wadekar**, M. Oevermann and A. Lipatnikov

Published in "SAE World Congress Experience", 2018, Detroit, USA

In this work, OpenFOAM libraries were extended to carry out Large-Eddy Simulations of an optical GDI engine for a motored and stratified mode operations. A turbulent flame speed closure model was implemented to simulate the flame propagation through inhomogeneous premixed reactants. The fuel injection process was modeled with a standard Lagrangian spray model. The laminar flame speed of the gasoline-air mixture was approximated as a function of the equivalence ratio, pressure, and temperature. The dependency of the burning rate on the local mixture was then determined. A presumed probability density function of the mixture-fraction was implemented to evaluate the influence of turbulent fluctuations of the mixture-fraction on the local burning rate. In general, the numerical solution confirmed that the above-mentioned implementations have a considerable effect on burning characteristics, such as the pressure evolution. The calculated pressure variations for three cases characterized by different loads, varying fuel injection, and spark timing were validated against experimentally recorded pressure traces. The simulated pressure evolution corresponded closely to the experimental results when a low load was considered but slightly over-predicted for the high load case. The increase in pressure obtained by considering fluctuations in the mixture fraction differed considerably from that obtained when fluctuations were ignored. However, with respect to the effect on the burning rate, the results revealed that variations in the mixture fraction had no effect with early fuel injection and a significant effect with late fuel injection. Furthermore, experimental images showing the location of the burned product associated with late fuel injection were accurately reproduced by the simulation.

Division of work: S. Wadekar developed the code, ran all the simulations, wrote the paper and generated all figures and tables. M. Oevermann was responsible for project acquisition and conceptualization, discussions, corrections and proof-reading. A. Lipatnikov contributed in conceptual work and discussion regarding the implementation of FSC model and other related models in OpenFOAM library.

Appendix

Figure 7.1 shows the injected fuel mass flow rate for a constant fuel mass (27 mg) at different injection pressures. The fuel injection duration for 1500 bar injection pressure was almost 60 % shorter than the 200 bar injection pressure. This mass flow rate profile is used as an input for the numerical calculations.

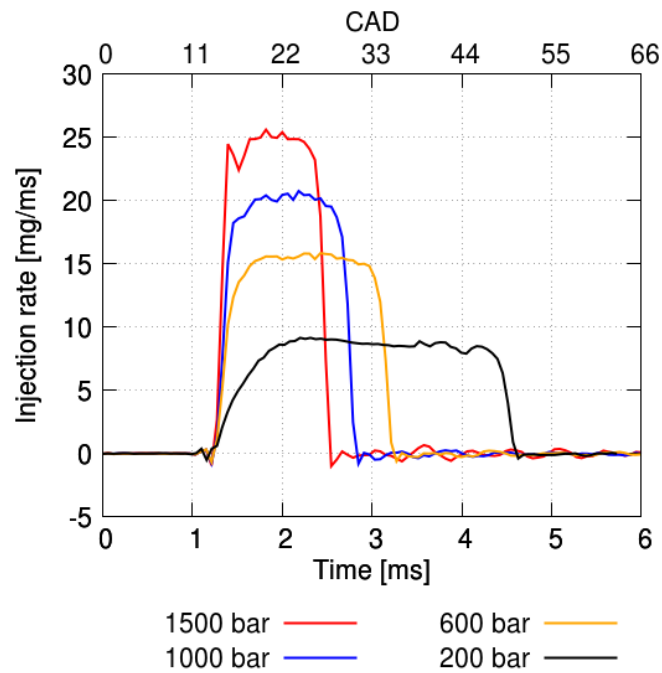


Figure 7.1: The fuel mass flow rate for a constant fuel mass at different injection pressures.

Figure 7.2 shows the time window used for the measurement of droplets mean sizes (D10 and D32). The time t_1 is signal delay time and t_2 is the needle opening time. In the post-processing of droplets sampling data, only the data of highlighted window is considered.

In the final empirical investigation, the effects of varying injection pressure on emis-

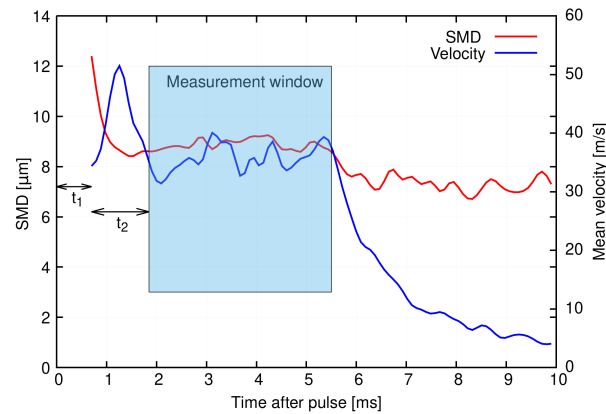


Figure 7.2: The time window for the droplets mean size measurement in divergent nozzle at 1000 bar injection pressure.

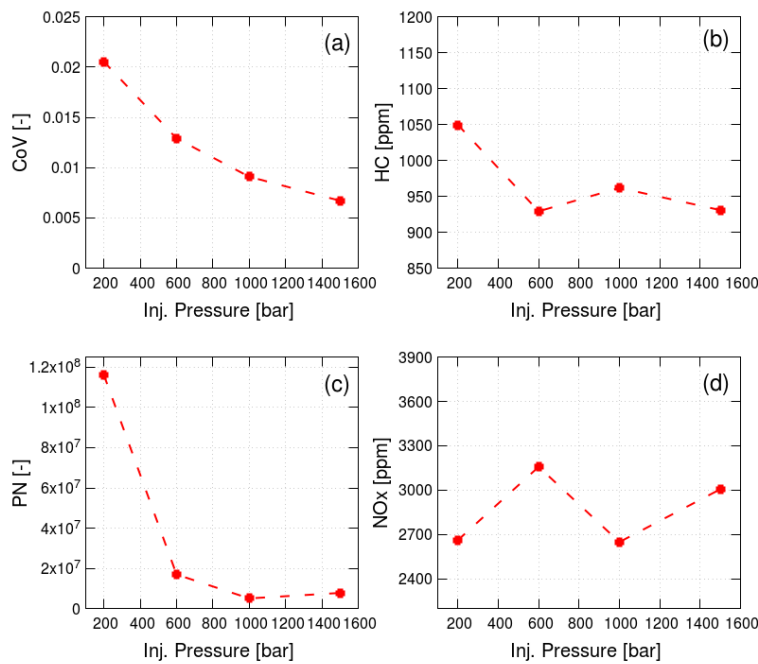


Figure 7.3: The results of emission data in a single cylinder metal engine measurement.

sions were analyzed using a single-cylinder metal engine test with similar specifications to the optical engine, and similar operating conditions, for a fair analysis. Some results of this measurement are presented in Figure 7.3. PN emissions were measured using a Cambustion DMS500 MkII Differential Mobility spectrometer, which enables measurements of particles with diameters up to 1000 nm. The particulate number was too low to detect with a volatile particle remover (which is usually used for

legislated PN measurements) so the DMS500 instrument was directly connected to the exhaust pipe, with its inlet positioned 200 mm downstream of the exhaust valve. Analysis of the particulate data acquired focused on > 10 nm particles.

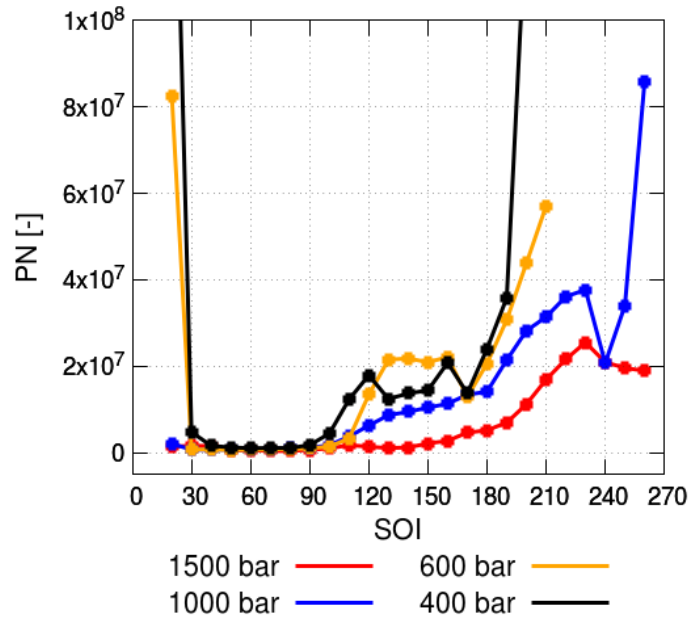


Figure 7.4: Comparison of PN emissions at indicated SOI timings and injection pressures.

Figure 7.4 shows the PN emissions at the selected injection pressures at various SOI timings. PN emissions were lowest with early injection timing (60 CAD) and highest with late injection timing. At all SOI timings, higher injection pressure resulted in lower PN emissions than lower injection pressure.

Bibliography

- [1] European-Commission, “Reducing co2 emissions from passenger cars”, URL https://ec.europa.eu/clima/policies/transport/vehicles/cars_en.
- [2] ICCT, “Reducing co2 emissions from passenger cars”, (2018), URL <https://theicct.org/publications/ldv-co2-stds-eu-2030-update-jan2019>.
- [3] Lipatnikov, A., Chomiak, J., “Turbulent flame speed and thickness: phenomenology, evaluation, and application in multi-dimensional simulations”, *Progress in Energy and Combustion Science* 28:1–74 (2002), URL [https://doi.org/10.1016/S0360-1285\(01\)00007-7](https://doi.org/10.1016/S0360-1285(01)00007-7).
- [4] Liang, B., Ge, Y., Tan, J., Han, X., “Comparison of pm emissions from a gasoline direct injected (gdi) vehicle and a port fuel injected (pfi) vehicle measured by electrical low pressure impactor (elpi) with two fuels: Gasoline and m15 methanol gasoline”, *Journal of Aerosol Science* 57:22–31 (2013), URL <https://doi:20.1016/j.jaerosci.2012.11.008>.
- [5] Chen, L., Liang, Z., Zhang, X., Shuai, S., “Characterizing particulate matter emissions from gdi and pfi vehicles under transient and cold start conditions”, *Fuel* 189:131–140 (2017), URL <https://doi:10.1016/j.fuel.2016.10.055>.
- [6] Mitroglou, N., Nouri, J., Yan, Y., Gavaises, M., “Spray structure generated by multi-hole injectors for gasoline direct-injection engines”, *SAE Technical Paper 2007-01-1417* (2007), URL <https://doi:10.4271/2007-01-1417>.
- [7] Piock, W., Befrui, B., Berndorfer, A., Hoffmann, G., “Fuel pressure and charge motion effects on gdi engine particulate emissions”, *SAE Int. J. Engines* 8:464–473 (2015), URL <https://doi:10.4271/2015-01-0746>.
- [8] Peer, J., Backes, F., Sauerland, H., Härtl, M., “Development of a high turbulence, low particle number, high injection pressure gasoline direct injection combustion system”, *SAE Int. J. Engines* 9:2301–2311 (2016), URL <https://doi:10.4271/2016-01-9046>.

- [9] Jones, T., “Assessment of technologies for improving light duty vehicle fuel economy: Letter report”, *The National Academies Press* (2010), URL <https://doi.org/10.17226/12163>.
- [10] Waltner, A., Lueckert, P., Schaupp, U., Rau, E., Kemmler, R., Weller, R., “Future technology of the spark-ignition engine: Spray-guided direct injection with piezo injector”, 27th *Vienna Motor Symposium* (2006).
- [11] Lee, S., Park, S., “Spray atomization characteristics of a gdi injector equipped with a group-hole nozzle”, *Fuel* 137:50–59 (2014), URL <https://doi.org/10.1016/j.fuel.2014.07.063>.
- [12] Chan, Q.N., Bao, Y., Kook, S., “Effects of injection pressure on the structural transformation of flash-boiling sprays of gasoline and ethanol in a spark-ignition direct-injection (sidi) engine”, *Fuel* 130:228–240 (2014), URL <https://doi.org/10.1016/j.fuel.2014.04.015>.
- [13] Song, J., Lee, Z., Song, J., Park, S., “Effects of injection strategy and coolant temperature on hydrocarbon and particulate emissions from a gasoline direct injection engine with high pressure injection up to 50mpa”, *Energy* 164:512–522 (2018), URL <https://doi.org/10.1016/j.energy.2018.09.011>.
- [14] Lee, Z., Park, S., “Particulate and gaseous emissions from a direct-injection spark ignition engine fueled with bioethanol and gasoline blends at ultra-high injection pressure”, *Renewable Energy* 149:80–90 (2020), URL <https://doi.org/10.1016/j.renene.2019.12.050>.
- [15] Kim, T., Song, J., Park, J., Park, S., “Numerical and experimental study on effects of fuel injection timings on combustion and emission characteristics of a direct-injection spark-ignition gasoline engine with a 50mpa fuel injection system”, *Applied Thermal Engineering* 144:890–900 (2018), URL <https://doi.org/10.1016/j.applthermaleng.2018.09.007>.
- [16] Du, J., Mohan, B., Sim, J., Fang, T., Roberts, W.L., “Experimental and analytical study on liquid and vapor penetration of high-reactivity gasoline using a high-pressure gasoline multi-hole injector”, *Applied Thermal Engineering* 163 (2019), URL <https://doi.org/10.1016/j.applthermaleng.2019.114187>.
- [17] Piock, W., Befrui, B., Berndorfer, A., Hoffmann, G., “Fuel pressure and charge motion effects on gdi engine particulate emissions”, *SAE Int. J. Engines* 8 (2015), URL <https://doi:10.4271/2015-01-0746>.

- [18] Peer, J., Backes, F., Sauerland, H., Härtl, M., “Development of a high turbulence, low particle number, high injection pressure gasoline direct injection combustion system”, *SAE Int. J. Engines* 9 (2016), URL [https://doi:10.4271/2016-01-9046](https://doi.org/10.4271/2016-01-9046).
- [19] Kim, K., Kim, D., Jung, Y., Bae, C., “Spray and combustion characteristics of gasoline and diesel in a direct injection compression ignition engine”, *Fuel* 109:616–626 (2013), URL <https://doi.org/10.1016/j.fuel.2013.02.060>.
- [20] Payri, R., García, A., Domenech, V., Durrett, R., Plazas, A.H., “An experimental study of gasoline effects on injection rate, momentum flux and spray characteristics using a common rail diesel injection system”, *Fuel* 97:390–399 (2012), URL <https://doi.org/10.1016/j.fuel.2011.11.065>.
- [21] Tian, J., Zhao, M., Long, W., Nishida, K., Fujikawa, T., Zhang, W., “Experimental study on spray characteristics under ultra-high injection pressure for diesel engines”, *Fuel* 186:365–374 (2016), URL <https://doi.org/10.1016/j.fuel.2016.08.086>.
- [22] Nauwerck, A., Pfeil, J., Velji, A., Spicher, U., “A basic experimental study of gasoline direct injection at significantly high injection pressures”, *SAE Technical Paper 2005-01-0098* (2005), URL <https://doi.org/10.4271/2005-01-0098>.
- [23] C, B., “Mixture formation in internal combustion engines”, *Springer-Verlag Berlin Heidelberg* (2016), URL <https://doi.org/10.1007/3-540-30836-9>.
- [24] Medina, M., Fatouraie, M., Wooldridge, M., “High-speed imaging studies of gasoline fuel sprays at fuel injection pressures from 300 to 1500 bar”, *SAE Technical Paper 2018-01-0294* (2018), URL [https://doi:10.4271/2018-01-0294](https://doi.org/10.4271/2018-01-0294).
- [25] Buri, S., “Effects of increased injection pressures of up to 1000bar – opportunities in stratified operation in a direct-injection spark-ignition engine”, *International Journal of Engine Research* 11:473–484 (2010), URL [https://doi:10.1243/14680874JER608](https://doi.org/10.1243/14680874JER608).
- [26] Imoehl, W., Gestri, L., Maragliulo, M., Del-Frate, L., “A doe approach to engine deposit testing used to optimize the design of a gasoline direct injector seat and orifice”, *SAE International Journal of Fuels Lubricants* 5:1078–1095 (2012), URL <https://doi.org/10.4271/2012-01-1642>.
- [27] Wetzels, J., “Optical analysis of the influence of injector hole geometry on mixture formation in gasoline direct injection engines”, *Automotive and Engine Technology* 1:57–67 (2016), URL <https://doi.org/10.1007/s41104-016-0005-1>.

- [28] Allocca, L., Lazzaro, M., Meccariello, G., Montanaro, A., “Schlieren visualization of a gdi spray impacting on a heated wall: Non-vaporizing and vaporizing evolutions”, *Energy* 108:93–98 (2016), URL <https://doi.org/10.1016/j.energy.2015.09.107>.
- [29] He, X., Ratcliff, M.A., Zigler, B.T., “Effects of gasoline direct injection engine operating parameters on particle number emissions”, *Energy & Fuels* 26:2014–2027 (2012), URL <https://doi.org/10.1021/ef201917p>.
- [30] Pan, H., Xu, M., Hung, D., Lv, H., “Experimental investigation of fuel film characteristics of ethanol impinging spray at ultra-low temperature”, *SAE Technical Paper 2017-01-0851* (2017), URL <https://doi.org/10.4271/2017-01-0851>.
- [31] VanDerWege, B., Han, Z., Iyer, C., Muñoz, R., “Development and analysis of a spray-guided disi combustion system concept”, *SAE Technical Paper 2003-01-3105* (2003), URL <https://doi.org/10.4271/2003-01-3105>.
- [32] Ferziger, J.H., Peric, M., “Computational methods for fluid dynamics”, *Springer-Verlag Berlin Heidelberg* (2002).
- [33] Wendt, J., “Computational fluid dynamics”, *Springer Berlin Heidelberg, Berlin, Heidelberg* (2009).
- [34] Hirschfelder, J., Bird, R., Curtiss, C., “Molecular theory of gases and liquids”, *Wiley* (1964).
- [35] Sutherland, W., “Lii. the viscosity of gases and molecular force”, *The London, Edinburgh, and Dublin Philosophical Magazine and Journal of Science* 36:507–531 (2009), URL <https://doi.org/10.1080/14786449308620508>.
- [36] Reynolds, O., “On the dynamical theory of incompressible viscous flows and the determination of the criterion”, *Philosophical Transaction of Royal Society* 186:123–164 (1894).
- [37] Davidson, P., “Turbulence: an introduction for scientists and engineers”, *Oxford University Press* (2015).
- [38] Richardson, L., “Weather prediction by numerical process”, *Cambridge (University Press)* (1922).
- [39] Pope, S., “Turbulent flows”, *Cambridge University Press* (2000).
- [40] Peters, N., “Turbulent combustion”, *Cambridge University Press* (2000).

- [41] Schmitt, M., Frouzakis, C., Tomboulides, A., Wright, Y., Boulouchos, K., “Direct numerical simulation of the effect of compression on the flow, temperature and composition under engine-like conditions”, *Proceedings of the Combustion Institute* 3 (2015).
- [42] Favre, A., “The equations of compressible turbulent gases”, *Technical report, DTIC Document* (1965).
- [43] Demirdžić, I., Lilek, Ž., Perić, M., “A collocated finite volume method for predicting flows at all speeds”, *International Journal for Numerical Methods in Fluids* 16(12):1029–1050 (1993), URL <https://doi.org/10.1002/flid.1650161202>.
- [44] Hoffmann, G., “Engineering application of large eddy simulation to turbulent free and wall-bounded shear layers”, *Universitaet Muenchen* (1995).
- [45] Smagorinsky, J., “General circulation experiments with the primitive equations”, *Monthly Weather Review* 91:99–164 (1963), URL [https://doi.org/10.1175/1520-0493\(1963\)091<0099:GCEWTP>2.3.CO;2](https://doi.org/10.1175/1520-0493(1963)091<0099:GCEWTP>2.3.CO;2).
- [46] Poinso, T., Veynante, D., *Theoretical and Numerical Combustion*, R.T. Edwards Inc., 2005, URL <https://hal.archives-ouvertes.fr/hal-00270731>.
- [47] Perini, F., Reitz, R.D., “Improved atomization, collision and sub-grid scale momentum coupling models for transient vaporizing engine sprays”, *International Journal of Multiphase Flow* 79:107–123 (2016), URL <https://doi.org/10.1016/j.ijmultiphaseflow.2015.10.009>.
- [48] Reitz, R.D., “Modeling atomization processes in high-pressure vaporizing sprays”, *Atomization Spray Technology* 3:309–337 (1987).
- [49] Tanner, F., Weisser, G., “Simulation of liquid jet atomization for fuel sprays by means of a cascade drop breakup model”, *SAE Technical Paper* 980808 (1998), URL <https://doi.org/10.4271/980808>.
- [50] Heywood, J., “Internal combustion engine fundamentals”, *McGraw-Hill* (1988).
- [51] Rolf, R., “Modeling spray atomization with the kelvin-helmholtz/rayleigh-taylor hybrid model”, *Atomization Spray Technology* (1999), URL <https://doi.org/10.1615/AtomizSpr.v9.i6.40>.
- [52] Gosman, A., Ioannides, E., “Aspects of computer simulation of liquid-fueled combustors”, *Journal of Energy* 7:482–490 (1983), URL <https://arc.aiaa.org/doi/10.2514/3.62687>.

- [53] Frössling, N., “The evaporation of falling drops (in german)”, *Journal of Geophysical Research* 52:170–216 (1949), URL <https://doi.org/10.1029/JZ054i004p00407-02>.
- [54] Torres, D., Trujillo, M., “Kiva-4: An unstructured ale code for compressible gas flow with sprays”, *Journal of Computational Physics* 219:943–975 (2006), URL <https://doi.org/10.1016/j.jcp.2006.07.006>.
- [55] Macpherson, G.B., Nordin, N., Weller, H.G., “Particle tracking in unstructured, arbitrary polyhedral meshes for use in cfd and molecular dynamics”, *Communications in Numerical Methods in Engineering* 25:263–273 (2009), URL <https://doi.org/10.1002/cnm.1128>.
- [56] Bai, C., Gosman, A., “Development of methodology for spray impingement simulation”, *SAE technical paper 950283* (1995).
- [57] Bai, C., Rusche, H., Gosman, A., “Modeling of gasoline spray impingement”, *Atomization Sprays* 12 (2002), URL <http://dx.doi.org/10.1615/AtomizSpr.v12.i123.10>.
- [58] Shim, Y., Choi, G., Kim, D., “Numerical and experimental study on effect of wall geometry on wall impingement process of hollow-cone fuel spray under various ambient conditions”, *Int J Multiphase Flow* 35 (2009), URL <http://dx.doi.org/10.1016/j.ijmultiphaseflow.2009.06.004>.
- [59] Montanaro, A., Malaguti, S., Alfuso, S., “Wall impingement process of a multi-hole gdi spray: experimental and numerical investigation”, *SAE technical paper 2012-01-1266* (2012).
- [60] Lucchini, T., D’Errico, G., Onorati, A., Bonandrini, G., Venturoli, L., Gioia, R., “Development of a cfd approach to model fuel–air mixing in gasoline direct injection engines”, *SAE technical paper 2012-01-0146* (2012).
- [61] Yamaguchi, A., Koopmans, L., Helmantel, A., Karrholm, F.P., Dahlander, P., “Spray characterization of gasoline direct injection sprays under fuel injection pressures up to 150 mpa with different nozzle geometries”, *SAE Technical Paper 2019-01-0063* (2019).
- [62] Weller, H.G., Tabor, G., Jasak, H., Fureby, C., “A tensorial approach to computational continuum mechanics using object-oriented techniques”, *Computers in Physics* 12:620 (1998), URL <https://doi.org/10.1063/1.168744>.

-
- [63] Janas, P., Wlokas, I., Böhm, B., Kempf, A., “On the evolution of the flow field in a spark ignition engine”, *Flow Turbulence and Combustion* 98:237–264 (2017), URL <https://doi.org/10.1007/s10494-016-9744-3>.
- [64] Lucchini, T., Della Torre, A., D’Errico, G., Montenegro, G., “Automatic mesh generation for cfd simulations of direct-injection engines”, *SAE Technical Paper 2015-01-0376* (2015), URL <http://doi:10.4271/2015-01-0376>.
- [65] Jasak, H., Tukovic, Z., “Automatic mesh motion for the unstructured finite volume method”, *Transactions of FAMENA* 30(2):1–20 (2006).
- [66] Pope, S.B., “Ten questions concerning the large-eddy simulation of turbulent flows”, *New Journal of Physics* 6:35–35 (2004), URL <https://doi.org/10.1088/1367-2630/6/1/035>.
- [67] Ritter, M., Malbec, L.M., Laget, O., “Assessment and validation of internal aerodynamics and mixture preparation in spark-ignition engine using les approach”, *SAE Technical Paper 2020-01-2009* (2020), URL <https://doi.org/10.4271/2020-01-2009>.
- [68] Lee, J., Goto, S., Tsurushima, T., Miyamoto, T., “Effects of injection conditions on mixture formation process in a premixed compression ignition engine”, *SAE Technical Paper 2000-01-1831* (2000), URL <https://doi:10.4271/2000-01-1831>.